

Physics of adhesion

W W Gerberich and M J Cordill

University of Minnesota, Chemical Engineering and Materials Science, 421 Washington Ave SE, Minneapolis, MN 55455, USA

Received 11 November 2005, in final form 23 May 2006

Published 26 June 2006

Online at stacks.iop.org/RoPP/69/2157

Abstract

Adhesion physics was relegated to the lowest echelons of academic pursuit until the advent of three seemingly disconnected events. The first, atomic force microscopy (AFM), eventually allowed fine-scale measurement of adhesive point contacts. The second, large-scale computational materials science, now permits both hierarchical studies of a few thousand atoms from first principles or of billions of atoms with less precise interatomic potentials. The third is a microelectronics industry push towards the nanoscale which has provided the driving force for requiring a better understanding of adhesion physics. In the present contribution, an attempt is made at conjoining these separate events into an updating of how theoretical and experimental approaches are providing new understanding of adhesion physics. While all material couples are briefly considered, the emphasis is on metal/semiconductor and metal/ceramic interfaces. Here, adhesion energies typically range from 1 to 100 J m⁻² where the larger value is considered a practical work of adhesion. Experimental emphasis is on thin-film de-adhesion for 10 to 1000 nm thick films. For comparison, theoretical approaches from first principles quantum mechanics to embedded atom methods used in multi-scale modelling are utilized.

This article was invited by Professor G T Gillies.

Contents

	Page
List of frequently used symbols	2159
1. Introduction	2161
2. Historical background and overview	2162
3. Friction and stiction of contacts	2164
4. Macroscopic, atomistic and mesoscopic modelling	2168
4.1. Definitions	2168
4.2. Macroscopic modelling (top-down)	2169
4.3. Atomistic modelling (bottom-up)	2172
4.4. Mesoscopic modelling (multi-scale)	2175
5. Experimental measures of de-adhesion and comparisons	2178
5.1. Four-point bending	2179
5.2. Indentation	2180
5.3. Stressed overlays	2182
6. Measures and comparisons	2184
6.1. Experimental measures	2185
6.2. Comparisons using mesoscopic modelling	2186
6.3. Comparisons using multi-scale modelling	2190
7. Summary and perspective	2193
Acknowledgments	2193
Appendix A. Pull-off forces for clean metal contacts	2193
Appendix B. Effect of interfacial dislocations on the work of adhesion	2194
Appendix C. Crack-tip dislocation emission and shielding	2195
References	2197

List of frequently used symbols

a	Contact radius of a sphere in contact
a_{ad}	Adhesive contact radius
α	0, 1 for JKR and DMT theories
α_1	Coefficient for strain gradient plasticity adhesion model
α_2	Buckling parameter for blister formation
B	Width of four-point bend specimen
b	Burgers vector of a dislocation
b_a	Blister/buckle crack radius after de-adhesion
β	Dimensional constant
β_σ, β_π	Bond energy integrals
β_{cu}	Proportionality constant for grain size strengthening
C	Plastic zone radius
c_{coh}	Contact radius plus cohesive zone size in pull-off
c_\perp	Dislocation free zone
D	Elastic half-strip height in SSV model
$D_{\text{F,S}}$	Plastic work of separation contributions from film and substrate
d	Grain size
δ	Normal displacement
δ_o	Critical displacement in a pull-off experiment
δ_b	Buckle height in blister/buckle formation
δ_f	Displacement at fracture
δ_{tip}	Crack-tip displacement
δ_\pm	Oscillation displacement
E	Elastic modulus
E^*	Reduced elastic modulus
E_{tip}	Elastic modulus for tip
E_s	Elastic modulus for sample
ε_f	Fracture strain
ε_\pm	Oscillatory strain
F	Friction force
\bar{F}	Normalized adhesion force
F_{ad}	Adhesion force during pull-off
F_c	Compressive force (load units)
G	Strain energy release rate (interfacial fracture energy)
G_I, G_{II}	Mode I and II strain energy release rates(interfacial fracture energies)
G_ψ	Mixed mode strain energy release rate(interfacial fracture energy)
$\gamma_\alpha, \gamma_\beta, \gamma_{\alpha\beta}$	Surface energies for materials α and β and between α and β incontact
$\gamma_\alpha^{\text{eq}}, \gamma_\beta^{\text{eq}}, \gamma_{\alpha\beta}^{\text{eq}}$	Comparable surface energies for materials α and β at equilibrium
γ^d, γ^p	Surface energies associated with London dispersion and polar forces
$\gamma_f, \gamma_s, \gamma_{fs}$	surface energies for film, substrate, and between film and substrate
H	Hardness or mean pressure
h	Film or layer thickness
K	Effective modulus used
K_I, K_{II}, K_{III}	Mode I, II, or III stress intensities

K_α	Positions of dislocations
k_{IE}	Local stress intensity for dislocation emission
k_{IG}	Local stress intensity for cleavage related to the Griffith energy
κ	Material constant for crack-tip dislocation shielding
L	Normal force in a friction experiment
λ	Length scale in strain gradient plasticity
λ	Normalized adhesion parameter
M	Bending moment
μ	Shear modulus of elasticity
μ_f	Friction coefficient
N_f	Number of cycles to failure
n	Strain-hardening exponent
ν	Poisson's ratio
ν_s	Poisson's ratio of the sample for indentation
ν_{tip}	Poisson's ratio of the indenter tip
ω	Constant (52.1°) used to calculate the phase angle of loading
P	Compressive load in indentation
$\Theta_{\sigma,\pi}^{ij}$	Bond orders
R	Indenter tip radius of curvature
R_{ij}	Bond lengths
R_p	Crack-tip plastic zone size
r	Radial distance from crack tip
r_c	Critical distance at which local stress exceeds friction stress
r_α, r_β	Interatomic or ionic radii of α, β materials
ρ	Indenter-induced dislocation density
ρ_c	Crack-tip dislocation density
σ_o	Adhesive stress in a cohesive zone
σ_o^{Cu}	Copper strength parameter
σ_f	Friction stress
σ_b	Critical buckling stress
σ_d	Driving stress for blister/buckle formation
σ_l	Indentation stress for blister formation
σ_{ys}	Yield strength
σ_{bond}	Bond strength
σ_{flow}	Flow stress
T_{kl}	External applied shear stress
τ_a	Interfacial shear strength
U_p	Plastic energy dissipation
U_{bond}	Bond energy
W_{ad}	Work of adhesion, adhesion energy
$W_{ad,P}$	Practical work of adhesion
W_{sep}	Work of separation
W_\perp	Stored energy of dislocations
ξ	Misfit parameter
ξ_b	Ratio of buckle height to film thickness
Ψ	Phase angle of loading

- Z_{α} Generic point when stress state is evaluated
 z_0 Equilibrium size of atoms in contact prior to de-adhesion

1. Introduction

About 1500 years ago the Damascus sword arrived on the field of battle and ever since has been the subject of countless folklore. The fabrication process involved folding over high carbon steel and forging the surfaces together until well adhered. This was then repeated multiple times. Still of interest today, a micrograph of adhered layers made by a combined torsional/damascene process is shown in figure 1. Analogous to this is the copper damascene process currently used in microelectronic interconnects in semiconductor technology. The main problem with the new technology early on was the adhesion of Cu lines to dielectrics. For this reason a burst of activity in the 1990s led to a number of techniques for determining interfacial fracture energies between metal films and silicon. This continues today as little is still understood about all the adhesion variables and their interactions.

Without an improved understanding of the physics of adhesion, devices manufactured by emerging technologies will increasingly fail. As examples, such issues are critical to microelectromechanical systems (MEMS), magnetic recording, transparent dielectric optical film and nanoparticle drug delivery systems. And this is only at the fabrication stage. Beyond that are wear, fatigue and stress corrosion issues, coupled to the adhesion problem which can delimit the lifetime of such devices in the field. Why should there be interest now, given the relative maturity of the microelectronics field? The nanotechnology mindset which pervades patents and processes of emerging technologies demands that scale-dependent properties be understood. As the physics of adhesion now covers more than ten orders of magnitude of scale, and the advent of scanning and tunnelling electron microscopes allows exploration of the lower force scales, great advances have been made. As an example of the magnitude of the scope of work at the smallest scale, a review [2] of modern nanotribology has 452 references covering atomic scale friction, adhesion and wear with some emphasis on dry adhesive contacts of AFM tips. Even this review covers a small subset of recent investigations associated with the physics of adhesion. This explosion of information is supplemented by research on additional phenomena which some would regard as cohesion. Consider the definitions that one might find in a dictionary [3].

- Adhesion. The molecular attraction that holds the surfaces of two dissimilar substances together.
- Cohesion. The molecular attraction or joining of the surfaces of two pieces of the same substance.

Two examples of adhesion and/or cohesion of steel surfaces illustrate the confusion that might arise with arbitrary definitions. First, take the extreme case of the driver being jolted by an unintended freeway stop after having a Jaguar transmission service without proper oil replacement. Assuming the meshing gears were of slightly different composition was this caused by adhesive or cohesive joining at the gear contacts? The second example concerns low-energy fracture along a grain boundary. Because of elemental phosphorus or sulfur segregation to a grain boundary, intergranular fracture may result at abnormally low forces. Is this adhesive or cohesive failure considering the compositional discontinuity at the grain boundary? This is considered to be an unnecessary nuance. For the purposes of this contribution, all forces required for separation of two substances brought into contact will be considered. Although all types of adhesive forces will be discussed, the emphasis will be restricted in scope. Consider the adhesion of a single contact with the surfaces schematically represented in figure 2(a).

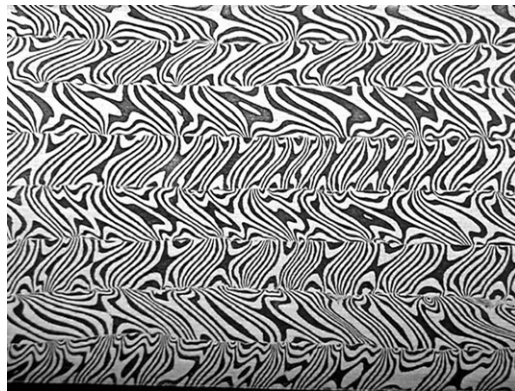


Figure 1. Modern Damascus sword process analogous to the copper damascene process used in microelectronic interconnects [1].

Such contact forces can increase from low values at self-assembled monolayers (SAMS) such as Langmuir–Blodgett films to larger values due to strongly adhered polymer chain networks. The latter might be relatively weak as in pressure sensitive adhesives (PSA) or stronger with interdiffusion of polymer microstructures. With increased bonding, adhesive forces for separation in crystalline materials can further increase from elastic debonding to elastic–plastic where local stresses become sufficient to move existing dislocations or create new ones. This is addressed for a nanocontact of about 10^4 nm^2 which might be a 50 nm radius nanodot or a 10 nm wide stripe about a micron long. For pulling such adhered contacts apart the forces and their associated contact adhesion stresses are given in figure 2(b). One sees that these forces may increase from a piconewton to millinewtons as the real area of contact and bonding increase. At the lower end only a few asperities within the 10^4 nm^2 area might be in contact resulting in small adhesion forces. Even with a full contact, however, increased bonding energies can have an enormous influence on adhesive forces. For the same nominal contact area, apparent adhesive strengths can vary from Pa to GPa stresses. Such a range depends on multiple phenomena involving at least four different mechanisms or types of adhesion. These will be cited briefly followed by the progress in the physics of adhesion predominantly concerned with the mechanisms associated with higher forces. The focus of this progress then will be the higher forces within the dashed box of figure 2(b). Additionally the focus will be on crystalline materials, predominantly metals, semiconductors and oxides, with further emphasis on the role of plastic deformation in de-adhesion.

First, a brief historical background and overview are considered. In the latter, information on adhesion topics not covered here are cited. Following that, adhesion of metal contacts, atomistic simulations of contacts and interfacial adhesion are examined in sequence. Finally, models and measurement for advancing the understanding of metal/semiconductor or metal/ceramic adhesion will be discussed.

2. Historical background and overview

Modern approaches to the physics of adhesion can be traced to the 1930s. Then, Bowden and Bastow examined the range of surface forces [3] and later with Leben [4], Moore and Tabor [5] examined the friction and adhesion of sliding metals. Nevertheless, adhesion, friction and wear mechanisms remained ill-understood even 50 years later. For example, as of 1984, Maugis and

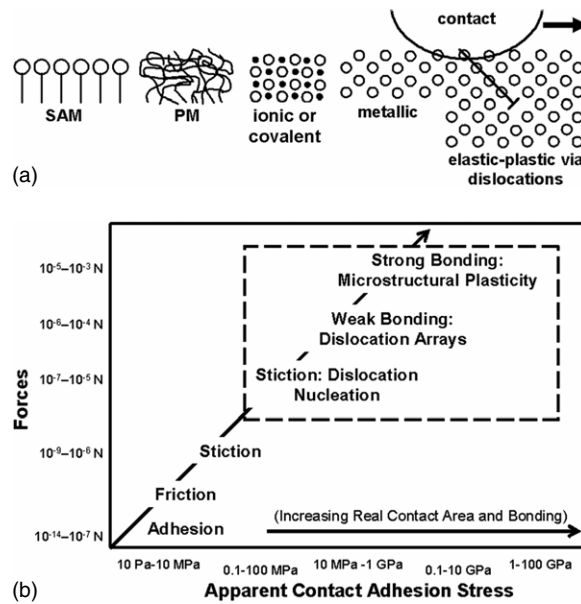


Figure 2. (a) Friction or adhesive forces would increase as contacts with self-assembled monolayers (SAMs), polymer microstructures (PM) such as pressure sensitive adhesives (weak) or block copolymers (strong) or ionic or metallic bonding without or with non-linear dissipation (dislocations) occurs. Note that the schematic is not to scale for a 10^4 nm² contact. (b) A large range of contact forces can result when pulling the contact of figure 2(a) off any of the indicated surfaces. The contact adhesion stress increases due to increasing numbers of asperities contacting such that the real-to-apparent area ratio approaches unity or the bonding forces increase. In turn, the number of non-linear energy dissipation mechanisms increases with increased bond energy.

Pollock [6] estimated that only 40 papers had appeared on the deformation and adhesion of metallic microcontacts. It was most prescient on their part when concluding that experiments were needed to determine whether or not single-asperity contacts resulted at low forces—two years prior to Binnig *et al.*'s [7] introduction of atomic force microscopy (AFM) in 1986. Since then the rate of publication has perhaps jumped by several orders of magnitude but not the rate of understanding.

The jump in the rate of publication is partially due to the diffusion of emphasis where research funding has gone from friction and wear to metal film adhesion to polymer adhesion to bioadhesion. AFM and associated scanning probe microscopy (SPM) techniques such as nanoindentation have provided much of the ability to gather experimental data. Theoretically the emphasis has gone down the scale from macro- to micro- to nanomechanics. This has involved macroscopic approaches using JKR [8] and DMT [9] theories of adhesion down to Lennard-Jones and more modern molecular dynamics techniques. Only within the last few years has there been much progress joining the experimentalist and theorist to understand deformation and fracture processes of importance to the physics of adhesion. An attempt will be made to bring into focus those multi-scale modelling efforts that can potentially lead to a broader understanding of the physics of adhesion.

As an overview, consider how the generalist might view adhesion. One can pick at least four categories of electrostatic, dispersive (van der Waals or London forces), chemical and diffusive bonding. Chemical, encompassing ionic, covalent and metallic bonds implies just nearest neighbor bonding across the interface while diffusive implies interpenetration of species

at relatively high temperature. To be sure interpenetration of polymer chains as a diffusive reptation process is important for adhesion of polymer surfaces [10, 11]. Furthermore, at very low mean contact pressures, van der Waals and London dispersion forces will dominate contact adhesion. It has been agreed upon that great insight has been gained into these two categories of very strong [12] and very weak adhesion [12] of biopolymer [13], glassy polymer [10, 11] and pressure-sensitive adhesives [14].

The main concerns here are regarding the two intermediate categories of dispersive and moderate chemical bonding. The goal is to convey an understanding of how the change in the strength of moderately bonded crystalline interfaces affects adhesion. As a result, it is proposed that the above four categories are not the best approach for establishing an understanding of the physics of adhesion. They are necessary to the understanding of bonding but not sufficient for establishing adhesion energies in either a theoretical or a practical sense. There is the true work of adhesion and the practical work of adhesion. Purely elastic contacts can be separated with the resultant measure being the true work of adhesion. Such measures have resulted in a time-honoured technique for measuring surface energies [8]. With even weak bonding, however, viscoelastic or plastic energy dissipation during contact separation can lead to enhanced practical works of adhesion. In this regard it is more than just the bonding that occurs at interfaces. It is the far-field effect away from the interface that may contribute the majority of the dissipative energy. For example, consider two adhesive bonds of sapphire to very thin films of niobium or tantalum nitride (Ta_2N). Both of these have a true interfacial bond energy on the order of 1 J m^{-2} for very thin films. Nevertheless, with increasing film thicknesses approaching $1 \mu\text{m}$, the measured adhesion energies would remain at 1 J m^{-2} for the Ta_2N films [15] but could increase to 10 J m^{-2} or more for the Nb film.

In the following nanocontacts are considered briefly at low adhesive forces and metal microcontacts at much larger forces. These directly lead to bottom-up strategies where large-scale computer simulations play an increasing role in multi-scale modelling.

3. Friction and stiction of contacts

Considerable progress has been made in the study of self-adhesion where forces for the contact area considered in figure 2(a) would be in the lower left corner of figure 2(b), i.e. the nanonewton¹ regime. Those studies which have been most informative deal with relatively small contact pressures and/or thin lubricating monolayers. Here, friction and stiction of such contacts have been the major subjects of books such as Israelachvili's *Intermolecular and Surface Forces* [16] and Maugis' *Contact Adhesion and Rupture of Elastic Solids* [17], where friction is defined as the force that opposes the motion of two surfaces in contact and stiction is the static friction between two surfaces not sliding. In the latter, Maugis shows that for frictionless elastic conical contacts that the adherence force is given by

$$F_{\text{ad}} = -54 \frac{W_{\text{ad}}^2 (1 - \nu^2)}{\pi E}, \quad (1)$$

with W_{ad} the adhesion energy, ν a Poisson's ratio and E an elastic modulus. This applies to a cone with a semi-angle of $\pi/4$. For a pressure-sensitive, adhering polymer surface with a surface energy of 30 mJ m^{-2} and a low modulus of 10 MPa , equation (1) represents an adherence force of 1 nN . For a considerably stiffer metal with a surface energy of 2 J m^{-2} and a modulus of 70 GPa , this is still an adherence force of about 1 nN . This value can be of great importance to stiction of cantilever devices proposed for MEMS devices. Further confirmation

¹ With larger contact areas as used in a surface forces apparatus [18], mN forces can be achieved with equally low contact stresses.

of that is in a recent study by Israelachvili [18] showing the importance of pico-scale topography for small forces. For friction force studies of molecularly thin attached monolayers to glass, they found the same value for Amonton's law of friction ($\mu_f = F/L = 0.3$), where F/L is the tangential to normal load ratio. The value of 0.3 persisted for both the surface forces apparatus where the pressure was on the order of a few MPa and the AFM where the pressure was a few GPa. As the AFM tip was silicon, such pressures approach the stress to nucleate a dislocation. They did find a friction transition and assumed it was a pressure-induced monolayer transition. From the shape of the transition curve, this appears to be the case but at much larger loads one may have to consider inelastic effects.

In the two recent aforementioned books [16, 17], two special journal issues [19] and several other contributions [20, 21], it is clearly documented that frictional properties [20–22], AFM pull-off forces [23] and chemical force microscopy (CFM) [24] can be controlled by weak forces. These references give a good overview of the physics of adhesion for the lower force/bonding aspects of surfaces, particularly with AFM-type contacts. The range of forces for nearly all papers was 1–300 nN with a few exceptions. In the context of figure 2(b), this represents the lower half of the force regime not considered extensively herein. Given the coverage of this low force regime, there is a complementary need to emphasize the higher force regime.

To this end, adhesion effects of such contacts are divided into two general regimes of interest, the first being mostly dependent upon nearest neighbor interatomic forces. Except for studies with the surface forces apparatus involving multiple contacts, these single point contact SPM studies deal with low forces.

For the second regime involving higher contact stresses, one example is a single point metal contact. These have been studied in vacuum or at larger contact compressive forces prior to pull-off in tension. Here, the bonding forces may be sufficiently great for the contact to approach the theoretical stress limit. Pethica and Tabor [25] were the first to study the contact of clean tungsten tips on clean ($\sim 2 \times 10^{-8}$ Pa vacuum) single crystal (111) planes of nickel. The tungsten tips had a radius of curvature of $R = 2 \mu\text{m}$. They found that with compressive loads, F_c , of increasing magnitude, subsequent pull-off forces or adhesion forces, F_{ad} , increased according to

$$F_{\text{ad}} = \beta F_c^{2/3}, \quad (2)$$

with β having the appropriate units. They found similar behaviour in crystals with a 5 nm thick oxide film after the oxide film was broken. Later Salmeron *et al* [26] demonstrated the same behaviour using AFM tips of Pt–Rh(13%) contacting into Au{111}. For Pethica and Tabor's [25] contacts involving a tungsten tip of radius $R = 2 \mu\text{m}$, this resulted in $\beta = 1.5 \mu\text{N}^{1/3}$ from their figure 2. At these low forces, if a near-Hertzian contact is assumed, equation (2) can be used to estimate the compressive contact force. This is then set equal to what might be expected for contacting spheres giving

$$\left(\frac{F_{\text{ad}}}{\beta}\right)^{3/2} \simeq \frac{4}{3} E^* R^{1/2} \delta^{3/2}, \quad (3)$$

with the right-hand side being the standard Hertz theory for a sphere contacting a plane. Here, R is the sphere radius, δ the displacement and E^* a reduced modulus given by

$$\frac{1}{E^*} = \frac{1 - \nu_{\text{tip}}^2}{E_{\text{tip}}} + \frac{1 - \nu_s^2}{E_s}. \quad (3a)$$

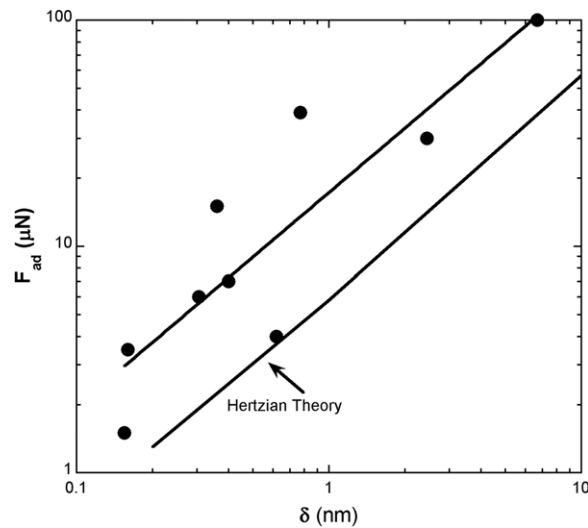


Figure 3. Hertzian theory can reasonably well predict the adhesion force versus geometric displacement for metal surfaces [25]. It also demonstrates Hertzian-like loads can be maintained with local plasticity of a few dislocations.

The elasticity parameters of ν_{tip} , E_{tip} and ν_s , E_s are Poisson's ratio and modulus for tip and substrate, respectively. This reduces to

$$F_{\text{ad}} \simeq \left(\frac{4}{3}E^*\right)^{2/3} \beta R^{1/3} \delta; \quad (4)$$

this is the linear relationship in figure 3 along with the reported adhesion force measurements [25]. The displacement was calculated from the contact diameter at pull-off. It is seen that the adhesion force is surprisingly well predicted by this Hertzian approach. There is a tacit assumption here that the contact radius at low forces is about the same at maximum compression, a_c , compared with that at adhesive pull-off, a_{ad} , in tension. This ratio of a_{ad}/a_c decreases somewhat at larger contact forces as outlined in appendix A. One immediately has to question why Hertzian-like forces, based on elasticity theory, can predict the result after plastic flow has commenced. Recently in compressing nanospheres and nanocubes [28, 29] as well as for very light nanoindentation into thin films [30], it has been shown that high internal back stresses from dislocation creation can assist in supporting loads equal to Hertzian. This partially explains the phenomenological relationship in figure 3 in two ways. First, it demonstrates that with local plasticity of the first few dislocations Hertzian-like loads can be maintained. This is shown in figure 4 for a 30 nm thick film of Ni. In figure 4(a) the dislocation emission of about 6 dislocations as indicated by the steps is seen to agree with residual plasticity. In figure 4(b), the experimental loading predicted by both a linear hardening model and Hertzian theory match well for the first 50 μN of load. Here, the indentation utilized a Berkovich-shaped diamond with a spherical tip of 303 nm radius. Elsewhere, it is shown that the hardening slopes in figure 4(a) can be predicted by simple dislocation pile-up theory postulated by Eshelby *et al* [31] a half-century ago. Second, it partially explains the puzzling feature that the adhesive forces in pull-off are only about a factor of two larger for a clean, well-bonded surface compared with a contact on a heavily oxidized (5 nm thick) surface that has not seen oxide breakthrough. One possible explanation follows. As mentioned above in equation (1), the adherence force for a surface energy of 2Jm^{-2} might only be a few

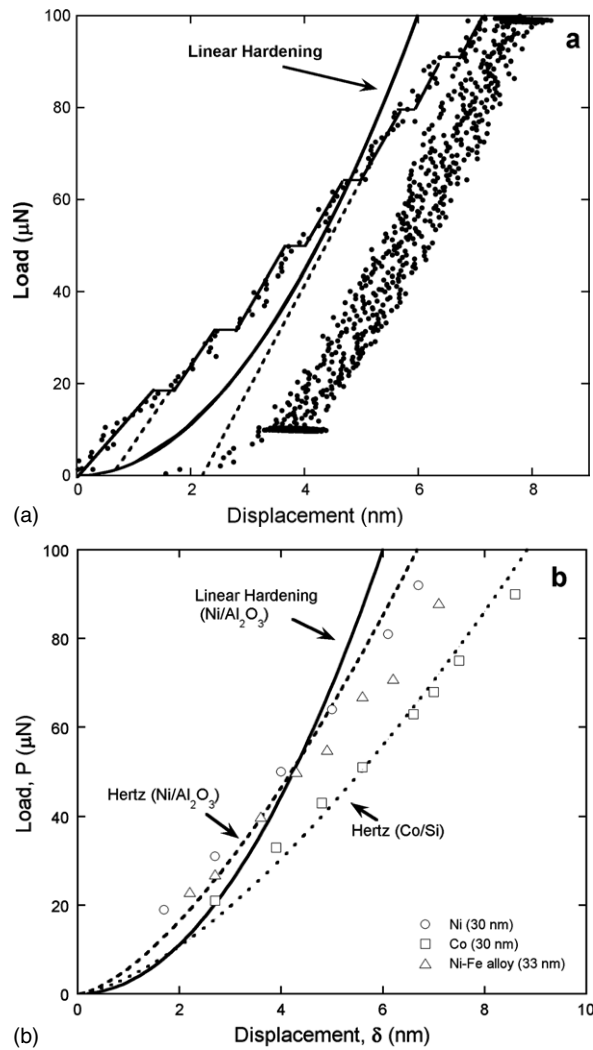


Figure 4. (a) load–displacement data for 30 nm Ni film with a linear hardening curve superimposed [32]. (b) supporting loads and displacements for the discretized displacement steps are shown along with Hertzian and linear hardening models for the 30 nm films (Ni, Co, $\text{Ni}_{80}\text{Fe}_{20}$) [32].

nN and not tens of micronewtons. Of course, equation (1) is for an elastic contact. It is strongly suggested that the dislocation structure created in the compressive contact creates a resistive back force on the indenter tip similar to a cohesive zone. This is schematically illustrated in figure 5. During pull-off the crack at either edge of the contact would tend to grow inwards. The crack growth is resisted by the dislocations created during the prior compressive loading. Given that the plastic zone radius for these light contacts would range between 100 and 300 nm, the nearest dislocations to the incipient crack tip would be very close. Even without breaking the oxide film, such linear arrays of dislocations could represent a clamping force resisting pull-off. As far as the authors know this is a totally unexplored regime of the physics of adhesion. Analogous behaviour for thin film adhesion is discussed in a subsequent section.

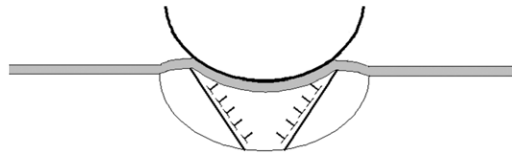


Figure 5. The schematic diagram strongly suggests that the dislocation structure created in the compressive contact creates a resistive back force on the indenter tip similar to a cohesive zone.

4. Macroscopic, atomistic and mesoscopic modelling

For any of the force or contact stress regimes illustrated in figure 2, the starting point for modelling is interfacial adhesion. Consider the contact of one solid, α , on another, β , in an environment equivalent to air. The work of adhesion as originally defined by Dupre (circa 1869) is defined by

$$W_{\text{ad}} = \gamma_{\alpha} + \gamma_{\beta} - \gamma_{\alpha\beta}, \quad (5)$$

where $\gamma_{\alpha,\beta}$ are for the surface energies of the two solids, separately, and $\gamma_{\alpha\beta}$ is the surface energy between the two materials in contact. Since the adhesion is only due to London dispersion forces, γ^{d} , and polar forces such as hydrogen bonding γ^{P} , Fowkes [33] has described the cross-term as

$$\gamma_{\alpha\beta} = \gamma_{\alpha} + \gamma_{\beta} - 2\sqrt{\gamma_{\alpha}^{\text{d}} \gamma_{\beta}^{\text{d}}} - 2\sqrt{\gamma_{\alpha}^{\text{P}} \gamma_{\beta}^{\text{P}}}. \quad (6)$$

It is clear from equations (5) and (6) that the works of adhesion only due to dispersion and polar forces would be

$$W_{\text{ad}} = 2 \left[\sqrt{\gamma_{\alpha}^{\text{d}} \gamma_{\beta}^{\text{d}}} + \sqrt{\gamma_{\alpha}^{\text{P}} \gamma_{\beta}^{\text{P}}} \right]. \quad (7)$$

This and other types of contacts which are most important to the contact of solids in a liquid environment are detailed by Leite and Herrmann [23]. For the present study where the majority of contacting films on substrates are deposited under partial vacuum and highly energetic forces such as argon bombardment, various degrees of chemical bonding result. Here, the work of adhesion will be referred to as

$$W_{\text{ad}} = \gamma_{\text{f}} + \gamma_{\text{s}} - \gamma_{\text{fs}}, \quad (8)$$

where $\gamma_{\text{f,s}}$ are the surface energies of the film and substrate, respectively, and γ_{fs} the surface energy between the two materials in contact after deposition.

Given the various levels of bonding possible from electrostatic to full cohesion, the approaches to modelling the physics of adhesion are manifold. First, a few definitions of general approaches are given and then each of these are applied to the levels of adhesion in figure 2, with special emphasis on the higher adhesive stress regime.

4.1. Definitions

Broadly classified macroscopic, atomistic and mesoscopic modelling will be considered as top-down, bottom-up and multi-scale models. With emphasis on thin-film adhesion of metal/ceramic or metal/semiconductor couples, these are defined as follows.

- Top-down. For almost all elastic contacts, regardless of their material type, the top-down approach utilizes the contact mechanics established by Johnson [27]. When adhesive forces become large as in well-adhered metal films, an inelastic approach is required.

Macroscopically, the mechanics of bi-material interfaces are understood [34]. From that it is inferred that increased plasticity, represented by mixed mode crack growth, can increase the fracture resistance. Mixed mode implies combinations of normal and shear displacement at a crack tip as discussed later. The knowledge of mode mixity is used to measure crack growth resistance using either four-point bending or indentation mechanics. For understanding film adhesion, a length scale approach involving both small-scale plasticity and crack-tip process zones is included.

- Bottom-up. From atomistic simulations bonding between dissimilar materials is beginning to be understood and will be able to predict how interfacial chemistry affects bond strength. For inelastic behaviour, this increase in adhesion will often be accompanied by dislocation emission out of the crack tip at much lower values of the local stress intensity than the Griffith value, i.e. $k_{IE} < k_{IG}$.

In a monolithic single crystal behaving elastically, the local Griffith stress intensity is $k_{IG} = (2E\gamma_s)^{1/2}$. This applies to cleavage along the most susceptible atomic plane, e.g. $\{100\}$ in BCC metals. For a bi-material, $2\gamma_s$ would be substituted by W_{ad} assuming the interface is at equilibrium. In many semiconductor, metal and oxide structures dislocation emission precedes fracture due to $k_{IE} < k_{IG}$. This is on a local scale. As will be seen on the macro scale, this requires larger applied stress intensities, K_I , for crack extension to occur. This is similar to plasticity-induced cleavage in body-centred-cubic materials near their brittle to ductile transition temperature [35].

- Multi-scale modelling approach. Coupled atomistic and discretized dislocation approaches will be able to integrate the top-down and bottom-up approaches. This requires a picture which appropriately includes the correct interatomic potentials for interfacial bond strength as well as the far field mechanics which affects the local shear stresses based upon dislocation densities and spatial arrangements.

Within these three broad categories, a few of the modelling efforts are described below.

4.2. Macroscopic modelling (top-down)

For elastic contacts there has been considerable progress and an acknowledgment in the field that JKR [8] and DMT [9] theories are applicable. A map due to Johnson [36] is reproduced in figure 6. Here, the normalized adhesion force, \bar{F} , and dimensionless scaling parameter, λ , are given by

$$\bar{F} = \frac{F_{ad}}{\pi W_{ad} R}, \quad (9a)$$

$$\lambda = 3.39 \left(\frac{W_{ad}^2 R}{K^2 z_0^3} \right)^{1/3}, \quad K = \frac{4}{3} \left(\frac{1 - \nu_1^2}{E_1} + \frac{1 - \nu_2^2}{E_2} \right)^{-1}, \quad (9b)$$

where z_0 is the equilibrium size of atoms in contact and K is an effective modulus associated with two elastic bodies having $E_{1,2}$ and $\nu_{1,2}$ elastic properties. The map in figure 6 shows a transition between DMT and JKR. This transition region can be formulated by a cohesive zone model postulated by Maugis [17]. The schematic in figure 7(a) shows the original contact radius, a_0 , is also the contact radius at zero load. With pull-off of the contact, the contact recession is like crack growth and the crack position advances with the remaining contact now having a radius, a . Because of the adhesion forces, there is a cohesive zone, $c-a$, with an opening displacement, δ_0 , at the edge. The clamping forces are represented by an adhesive stress of σ_0 in the cohesive zone. The work of adhesion is then represented by $\sigma_0 \delta_0$ with the rectangular force-displacement law in figure 7(b). The radius, a , at pull-off will decrease the

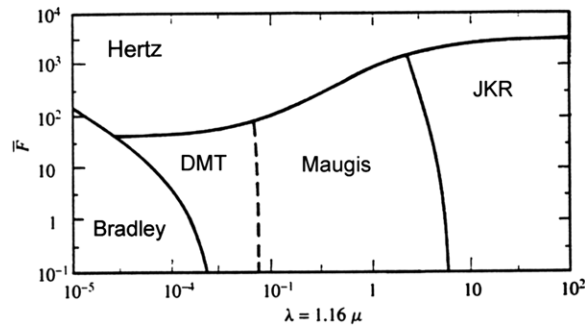


Figure 6. JKR-DMT transition represented by equations (9a) and (9b). The relationship between contact area and load for an elastic sphere contacting a plane depends upon the range of attractive surface forces. Area-load curves for the JKR limit (short-range adhesion), DMT limit (long-range adhesion) and an intermediate case are shown. All of these approach the Hertz curve in limit $\gamma \rightarrow 0$ (no adhesion). Load and area are plotted in non-dimensional units as indicated. Reprinted from *Tribol. Int.* **31** and K.L. Johnson 1999 *Mechanics of Adhesion* pp 413–18, with permission from Elsevier [36].

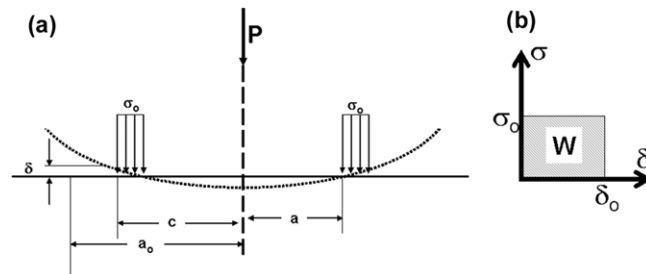


Figure 7. (a) The original contact radius, a_0 , is also the contact radius at zero load. With pull-off of the contact, the contact recession is like crack growth and the crack position advances with the remaining contact now having a radius, a . The clamping forces are represented by an adhesive stress of σ_0 in the cohesive zone. (b) The work of adhesion is then represented by $\sigma_0 \delta_0$ with the rectangular force–displacement law.

stronger the adhesion force. Carpick *et al* [37] developed a simple model for applying these types of contacts to friction studies. This gave

$$\frac{a}{a_0^\alpha} = \left[\frac{\alpha + \sqrt{1 - P/F_{ad}^\alpha}}{1 + \alpha} \right]^{2/3}, \quad (10)$$

where $\alpha = 0$ for the DMT theory and $\alpha = 1$ for JKR. The adhesion forces, F_{ad} , are $2\pi RW_{ad}$ for DMT and $(3/2)\pi RW_{ad}$ for JKR. One can show that this is applicable for forces in the nanonewton regime for small contacts less than 10 nm. However, for forces much larger than 1 μN , this is no longer applicable as $P > F_{ad}^\alpha$. For the types of forces represented by elastic contacts in figure 2, one can show for relatively soft materials with $K \sim 1 \text{ GPa}$ and $W_{ad} \sim 2 \text{ J m}^{-2}$ that $\lambda \sim 4$. This represents a maximum adhesion force of about 10 μN for a 100 nm radius tip. For much larger forces between elastic contacts adhesion is negligible for the size of contact considered here.

For an elastic–plastic contact both Maugis and Pollock [6] and more recently Mesarovic and Johnson [12] have utilized the same schematic as shown in figure 7. The adhesion force

for the former has been given by Biggs and Spinks [38] to be

$$F_{\text{ad}} = \frac{3\pi W_{\text{ad}}}{2(\pi H)^{3/2}} P^{1/2}, \quad (11)$$

where H is the hardness or mean pressure. For the same set of the above given parameters, again the adhesion force is usually substantially less than $10 \mu\text{N}$.

As stated above in the overview, the higher stiction and friction force regime associated with strong bonding can lead to forces in the μN to mN regime. This starts to be of interest to the adhesion of thin films where interconnect lines of 10 nm width can be debonded by tangential loads as small as $1 \mu\text{N}$. The top-down mechanics approach has been two-fold, one describing the mechanics adequately so that adhesion measurements can be made and the second utilizing various length scale models to predict elastic–plastic debonding of thin films. The first will be described in section 5 under the mechanics techniques for measuring adhesion energies. Predictive modelling evolved partly out of the need to understand the very large adhesion energies that could result during interface separation. Additionally, it was observed that an increase in toughness occurred by utilizing a mixed mode loading with increased amounts of shear, e.g. larger ratios of mode II, in-plane shear, compared with opening mode I loading [39,40]. Top-down modelling could accommodate elastic–plastic modelling at sharp interfaces using a continuum plasticity region contiguous to an elastic strip of height, $2D$, which was dislocation-free. This was conceptualized in the SSV model by Suo *et al* [41], as a way to account for cleavage cracking in the presence of plasticity. In the context of mesoscopic modelling which will be discussed later, this is analogous to dislocation models with a dislocation-free zone at the crack-tip. This elastic-strip model seemed consistent with the large toughness increases in interface separation compared with the work of adhesion for atomic separation. About the same time that the SSV model was being developed, Elssner [42] demonstrated that the macroscopic work of fracture between Nb and Al_2O_3 increased by 2–3 orders of magnitude beyond W_{sep} for the atomic work of separation.² This was not a crack-tip blunting effect as the crack-tip remained atomically sharp. In the same time frame, Wang *et al* [43] and Venkataraman *et al* [44] demonstrated a similar increase in the practical work of adhesion of metal/ceramic interfaces with increasing metal-film thickness. For example, in $\text{Ti}/\text{Al}_2\text{O}_3$ interfaces, the work of adhesion as measured by both microscratch and four-point bending increased from 0.3 to 90 J m^{-2} as thicknesses increased from 100 nm to $100 \mu\text{m}$, a factor of 300 increase in toughness [43,44].

As was stated, these types of measurements were coupled to a number of macroscopic modelling approaches starting with Needleman [45], Rice [39] and Tvergaard and Hutchinson [40], culminating with the SSV model of Suo *et al* [41], to name a few. As applied to the effect of plasticity on the crack growth resistance of an interface, this utilized two length scale parameters of the elastic strip and the plastic zone. Typically the elastic strip was taken to be on the order of 100 nm or greater. Later it was recognized that plasticity near a crack-tip could be at a finer scale. Additional macroscopic modelling involved strain gradient plasticity models [46–49]. Lipkin *et al* [47] and Huang *et al* [49] were two of the first researchers to use such approaches. Both recognized the need for a self-consistent description of the non-linear coupling that existed between cleavage separation and the surrounding plasticity. Strain gradient plasticity provides such an approach if it is mechanism-based. Such an approach allows for an internal length scale, λ which can be related to a flow strength [47], σ_{flow} ,

² Some authors appropriately choose to define a difference between the work of adhesion, W_{ad} , an equilibrium thermodynamic quantity, and the work of separation, W_{sep} , a non-equilibrium quantity. This is further addressed in the next section.

given by

$$\ell = 10\mu b/\sigma_{\text{flow}}, \quad (12)$$

with μ and b the shear modulus and burgers vector of the material. Even for flow stresses approaching $\mu/10$ near the theoretical strength limit, this gives an elastic core size of $100b$ which is greater than the approach of the nearest dislocations to the crack-tip for relatively thin films of several hundred nanometres or less [50]. Nevertheless, for thicker films this may represent a reasonable approach for elastic–plastic de-adhesion. As a review of mechanism-based strain gradient (MSG) plasticity, Jiang *et al* [48] have emphasized that MSG plasticity governs crack-tip behaviour at distances larger than λ . A further caveat for the use of such models is they do not adequately consider dislocation emission from the crack tip. As recognized by the larger community, further progress requires a more robust local picture of microstructural evolution at and near a crack-tip. Partly for that reason and partly for the increased capacity of large-scale computation, atomistic models have increased their role in crack-tip modelling.

4.3. Atomistic modelling (bottom-up)

Two types of atomistic modelling of importance to further progress are those dealing with both structure and chemistry of interfaces and those dealing with dislocation structures at or near interfaces. A complete review of such approaches is not possible here but many of the types that have been utilized will be indicated.

Prior to discussing these atomistic simulations, it should be recognized that much can still be learned from approaches used to establish phase boundaries. For example, Becker [51] used an interfacial broken bond model and Lee and Aaronson [52] developed a discrete lattice plane analysis based on this approach. Becker's [51] model was further extended by Borchers and Bormann [53] to determine low-temperature interfacial energies. For example, $\gamma_{\alpha\beta}$ for Fe–Ag was 0.86 J m^{-2} compared with a high temperature experimental value of 1.04 J m^{-2} . Similarly, for Cu–Co they found $\gamma_{\alpha\beta}$ to be 0.32 J m^{-2} compared with experimental values of about $0.230 + 0.30 \text{ J m}^{-2}$. Such thermodynamic approaches should be consistent with the interfacial energies determined by molecular dynamics simulations. There is some concern here since many, if not most, atomistic [54, 55] and 'macroscopic atom' models [56] have shown atomistic simulations to give energies greater than experimental values.

In the following there are 21 data sets from four theoretical simulations [55–59] and 13 data sets collected from several de-adhesion experiments involving the mechanical work of separation [55, 60–62]. This will still be designated W_{ad} as related to equation (5) but to be clarified below. In figure 8, W_{ad} is shown as a function of a misfit parameter. This crude misfit parameter is given in terms of radii (r_{α} , r_{β}) at the interface,

$$\xi = \frac{r_{\alpha} - r_{\beta}}{r_{\alpha}}, \quad (13)$$

with r_{α} being the larger of the two species.

The misfit parameter is an oversimplistic interatomic radii misfit for metals. Where reactive species are involved, e.g. oxides, ionic radii misfits are used. The top three groupings are all theoretical works of adhesion, the first by Bennet *et al* [56] using a macroscopic atom model, the next two by Siegel *et al* [57, 58] and Reynolds *et al* [59] using self-consistent density functional (DFT) calculations. The top grouping is concerned with NiAl in contact with Hf, Y, C or S [56] or a NiAl/Mo interface as is or with C, O or S at the interface [59]. The next grouping comes from the macroscopic atom model [56] for Al_2O_3 in contact with Hf, Zr, NiAl, Y, S, C, HfO_2 , ZrO_2 and Y_2O_3 . The DFT simulations representing carbides and nitrides

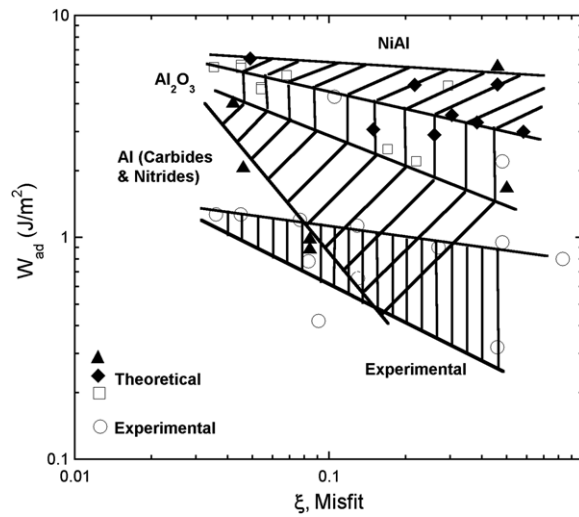


Figure 8. Graph illustrating that both macroscopic models and atomistic simulations can give similar answers and trends, emphasizing the misfit parameter is not fundamental and only meant for illustrative purposes.

are for Al contacts with WC, VN and VC but with various terminations, e.g. the aluminium in contact with either carbon or tungsten atoms for the tungsten carbide top layer [57, 58]. For each case there was at least one major outlier. The importance of figure 8 is two-fold, the first being to demonstrate that both macroscopic models and atomistic simulations can give similar answers and trends, emphasizing this misfit parameter is not fundamental and only meant for illustrative purposes. In that context, there is very little information on metal/carbide or metal/nitride interfaces from what is available and there may be little, if any, trend with ξ .

The second point was to demonstrate that at least for the oxide and metal references selected [55, 60–62], there appeared to be a trend for interfacial energy to decrease with increasing misfit but a very weak dependence. More important for the 34 points represented here are that only 2/13 experimental points were above the top trend line of the experimental data and only 2/21 of the theoretical determinations were below the same trend line. Admittedly, other experimental data could have been presented where interfacial ‘glue’ was purposely placed at the interface to improve bonding as needed by the microelectronic industry. Without that extraordinary effort, however, there appears to be a general disconnect between measured values and calculated values. As mentioned above, there can be differences between W_{ad} and W_{sep} . In an elegant and detailed study using first-principles calculations, Batyrev *et al* [55] showed that the work of separation, W_{sep} of Nb/sapphire interfaces, could depend upon the cleavage plane as well as the terminating surface atoms prior to adhesion. For nine different combinations, the relaxed values of W_{sep} ranged from 2.7 to 12.7 J m⁻². They equate these values with the Dupre work of adhesion (equation (4)) but emphasize that this interfacial energy for the work of separation is different from the interfacial energy associated with the work of adhesion,

$$W_{ad} = \gamma_{\alpha}^{eq.} + \gamma_{\beta}^{eq.} - \gamma_{\alpha\beta}^{eq.} \quad (14)$$

The reason is that these three total energies are in equilibrium whereas created interfaces in a given environment of partial pressure are not in equilibrium. Since nearly all processed thin films in commercial environments are non-equilibrium, W_{sep} is more important to the issue of interfacial fracture. They do show for this case of Nb/Al₂O₃ that $W_{sep} > W_{ad}$

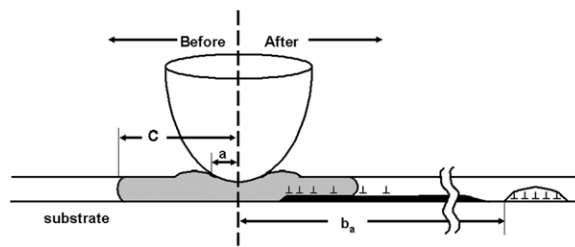


Figure 9. As a circular delamination is initiated and then grows to form a blister, dislocations are emitted. Half-section depictions of before initiation and after crack arrest are shown. In both cases the dislocation structures represent a substantial part of the work of adhesion representing much of the discrepancy in figure 8.

for nine different arrangements of interfacial atoms and various partial pressures of oxygen. This by itself does not explain the disconnect illustrated in figure 8. In an earlier work, Finnis [54] estimated the work of separation of Ag/MgO from the calculations of Schönberger *et al* [63], combined with experimental data for the MgO surface energy, to be 0.9 J m^{-2} . The calculations alone gave simulated values of $1.7 \pm 0.1 \text{ J m}^{-2}$ for W_{sep} . This nearly factor of two difference was not explained. They suggested that theoretical values of W_{sep} could exceed experimental estimates since misfit dislocations in the latter would reduce measured values. The reduction would be related to the density area of dislocations times their line energy. Based on Gumbsch's [64] 1991 estimates of misfit dislocations using embedded atom approaches, they found this could only account for about 10% of the discrepancy. However, in the vast majority, if not all, of metal/ceramic or metal/semiconductor interfaces, mechanical measurements cause considerable emission and/or evolution of dislocation structures prior to and coincident with separation [50]. In very thin films or nanostructures these densities may be quite high.

Such a calculation is shown in appendix B for an indentation-induced delamination, described more fully in section 5. The initiation of such a delamination accompanied by plasticity could produce substantial dislocations. As a circular delamination is initiated and then grows to form a blister more dislocations are emitted. These two events are estimated in appendix B for initiation and arrest. Dislocation densities for the case cited could be 10^{15} m^{-2} at initiation and 10^{14} m^{-2} at arrest. This is illustrated by the schematics in figure 9 where half-section depictions of before initiation and after crack arrest are depicted. In both cases these dislocation structures represent a substantial part of the work of adhesion representing much of the discrepancy in figure 8. As such estimates are replete with assumptions, careful multi-scale modelling as described in the next section is essential for progress in understand this aspect. The other aspect of figure 8 that needs additional discussion is that the dislocation structure emitted from the crack tip is beneficial as well as detrimental. While the defect structure may compromise the bonding across the interface it can be far more beneficial by providing crack-tip shielding, thereby retarding crack instability. This is expanded upon in the next section which addresses mesoscopic modelling.

Prior to that, it is appropriate to mention other atomistic simulation approaches of importance to understand mesoscopic structures even though they have not addressed adhesion issues or crack problems. Three other atomistic simulations of dislocations at or interacting with interfaces are by Swygenhoven *et al* [65], Yamakov *et al* [66] and Hoagland *et al* [67]. The first two deal with dislocation nucleation at grain boundaries in nanocrystalline [65] FCC Cu, Ni and Al [66]. The third simulates the resistance of interfaces, both strong and weak,

to dislocation interactions in multilayer structures [67]. In the first, a molecular dynamics code used tight binding in Parrinello–Rahman’s method and in the second two embedded atom method potentials (EAM) used up to 10^6 atom simulations. In particular, Yamakov *et al* [66] demonstrated partial dislocation separation effects on dislocation nucleation and an internal back stress that produced reverse plasticity. Both these phenomena have implications on multi-layer film systems that might undergo repeated contacts in technical devices. Hoagland *et al*’s study [67] also addressed dislocations at or near interfaces but in the context of whether the interface is well-bonded as in coherent or semi-coherent or not so well bonded as in incoherent. They prefer to label the Cu/Ni and Cu/Ag as transparent interfaces and the Cu/Nb as an opaque interface. The approach has to do with the shear strength of the interface and whether interface sliding or dislocation transmission might result. One result for Cu/Nb which can be epitaxial $\langle 110 \rangle_{\text{fcc}} || \langle 111 \rangle_{\text{bcc}}$ is (nevertheless) relatively opaque. They demonstrate that the interface exhibits stick–slip sliding at $\tau \sim 0.55$ GPa, whereas the theoretical shear strength for Cu is $\tau_{\text{theo.}} \sim 5$ GPa. Incorporating such details will be necessary to evaluate evolutionary dislocation structures that can interact with cracks and interfaces as simulated by the multi-scale models described in the next section.

4.4. Mesoscopic modelling (multi-scale)

Mesoscopic refers to the middle-ground plasticity effect on de-adhesion. As implied in the overview, it is neither the microstructural effect on the work of separation at the atomistic end nor the continuum plasticity effect that might apply to far-field regions from the interface. Rather, it is the dislocation structure, both density and spatial arrangement, that affects the work of separation. In this discussion and in the experimental information to follow based upon mechanical measurements, it will be assumed $W_{\text{sep}} = W_{\text{ad}}$ as defined by equations (5) and (9a) even though these are non-equilibrium quantities. There are two mesoscopic approaches which have dominated to date. One deals with simple, idealized arrays of a few dislocations that can be handled by interactive codes with either static [68] or dynamic conditions [69]. These have generally involved dislocation emission at the crack tip [68] or near it [69]. The other type typically involves larger simulation codes with many external sources randomly placed by a Voronoi tessellation [70]. Alternatively, these larger simulation codes can provide for dislocation generation in a small region contiguous to a crack-tip, then, with a handshake to a far-field continuum region modelled by finite elements, simulate large-scale effects. These are called quasi-continuum models [71–73] but are generally referred to as multi-scale models which can include atomistic, microstructural and continuum plasticity in a single simulation.

The first type evolved out of both experiment and theory, and these will be called dislocation-free zone (DFZ) models even though the concept of a DFZ is somewhat of a misnomer. At the crack-tip of reasonably high strength materials with a large number of dislocations present the so-called DFZ may only be 10 nm in size. Calling this region dislocation-free has been questioned by experimentalists even though there must be agreement that the crack-tip stress field strongly adjusts the dislocation region contiguous to the crack-tip. With the nearest tip-emitted dislocation being pushed away by the crack-tip stress field, this DFZ becomes a critical length scale in modelling fracture resistance. These and similar crack-tip source models [74–81] were generally directed towards cleavage phenomena in relatively brittle materials. Later on they were applied to layered structures [75] and thin films [81].

In a coarse-grain polycrystalline material, the nearest dislocation might be a 100 nm or more from the crack tip as illustrated in figure 10(a). In thin films or layered structures, it may be even closer as indicated in figure 10(b). This is partially due to interface trapping of the slip bands, for example, in a thin film of thickness, h . Here a 100 nm film may be trapped on

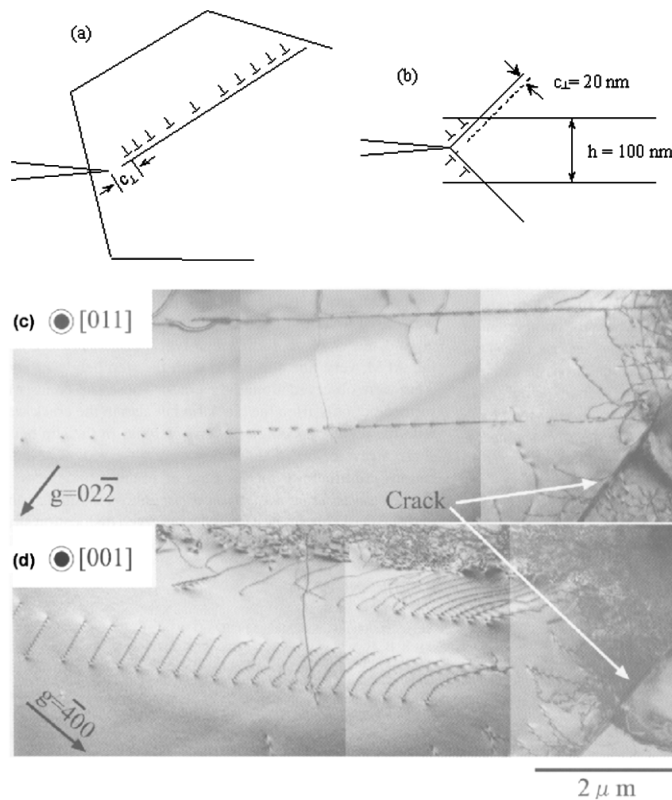


Figure 10. Dislocation shielding showing (a) a schematic with a dislocation-free zone, c_{\perp} ; (b) that thin films of thickness, h , may have dislocations blocked by a substrate or passivation films; (c) an emitted shielding pileup from a crack tip in silicon imaged with a $022g$ vector in TEM and (d) imaged with $g = 400$ (After Tanaka *et al* [82]). Note that the nearest dislocation is on the order of 100 nm from the crack tip.

one side by the substrate and on the other by a passivation film or native oxide as often occurs in microelectronic film stacks.

An example similar to this for dislocations emitted at the tips of cracks in a silicon single crystal has been evaluated by Tanaka *et al* [82]. These are shown at a Vickers indentation in figures 10(c) and (d). The crack nucleated at room temperature showed no evidence of dislocations, but upon increasing the temperature to 823 K, dislocation arrays were formed as indicated in figures 10(c) and (d). Analysis showed that the dislocation arrays represented a shielding stress intensity of $-0.722 \text{ MPa m}^{1/2}$. Of note is that this shielding stress intensity is equivalent to the fracture toughness of bulk silicon in tension which is about $0.7 \text{ MPa m}^{1/2}$ at room temperature.

For the adhesion subject at hand, only a few attempts at adapting this type of modelling have been made. Semi-quantitatively, it is useful to illustrate three of these dislocation shielding effects on improving the de-adhesion resistance. Both static [68] and dynamic [69] simulations generally evolved out of a series of contributions by Thomson [74,75] on the physics of fracture. For a strain-hardening material, Thomson [75] determined that the crack-tip stress was shielded from the far-field stress intensity, K_I , by the nearest dislocation separated by a distance, c_{\perp} ,

the DFZ. This gave

$$K_I = \kappa \left(\frac{k_{IG}^2}{c_{\perp}} \right)^{(1+n)/4n}, \quad (15)$$

where κ represents material properties and the local stress intensity, k_{IG} , was related to the Griffith energy for cleavage, G_I , by

$$G_I = k_{IG}^2/E. \quad (16)$$

From a series of papers utilizing the Atkinson and Clements [76] formalism for crack-tip/dislocation stress field interactions, Lii *et al* [77–79] and Gerberich and co-workers [81, 83, 84] demonstrated that a static solution for crack-tips stabilized by a crack-tip emitted dislocation array was [81]

$$K_I = \sigma_{ys} \left[\frac{2c_{\perp}}{\pi e^{4/3}} \right]^{1/2} \exp \left[\frac{\pi^{3/2} k_{IG}}{6\sqrt{2}c_{\perp}\sigma_{ys}} \right]. \quad (17)$$

For those not familiar with the equilibrium of forces concept associated with shielding, an abbreviated synopsis is given in [appendix C](#).

As mentioned earlier, another approach to resolve the local length scale problem was to use strain gradient plasticity theory [46]. Although more macroscopic in approach compared with discretized dislocation models, this produced an interestingly similar result to equation (15), namely,

$$G_I = \alpha_1 W_{ad} \left(\frac{W_{ad}}{b\sigma_{ys}} \right)^{(1-n)/n}. \quad (18)$$

Since W_{ad} for non-equilibrium materials is the Griffith energy for the interface, pure mode I loading³ from equations (15)–(18) give

$$G_I = \frac{\kappa^2}{E} \left(\frac{k_{IG}^2}{\sigma_{ys} E c_{\perp}} \right)^{(1+n)/2n}; \quad (19a)$$

$$G_I = \frac{2\sigma_{ys}^2 c_{\perp}}{E \pi e^{4/3}} \exp \left[\frac{\pi^{3/2} k_{IG}}{3 \sigma_{ys} \sqrt{2} c_{\perp}} \right]; \quad (19b)$$

$$G_I = \alpha_1 \frac{k_{IG}^2}{E} \left(\frac{k_{IG}^2}{\sigma_{ys} E b} \right)^{(1-n)/n}. \quad (19c)$$

For an example, consider the following parameters for a thin film of strain-hardening material de-adhered at k_{IG} . Then, the question is asked as to what the impact would be if the work of separation at the interface, W_{ad} , was quadrupled. Stated in terms of the Griffith relationship, equation (16), this would be a doubling of k_{IG} . The example material is defined as in the following table.

$E = 100 \text{ GPa}$	$c_{\perp} = 10 \text{ nm}$	$k_{IG} = 0.4 \rightarrow 0.8 \text{ MPa m}^{1/2}$
$\sigma_{ys} = 1 \text{ GPa}$	$n = 0.2$	$\kappa, \alpha_1 \text{ unspecified}$

For the three models of equation (19), quadrupling the interfacial work of separation (which doubles k_{IG}) would, respectively, result in a factor of 64, 200 and 1000 increase in the far-field G_I . This global G_I value is the practical work of adhesion effectively. The large increase is due to the local bond strength being able to support higher stresses and, hence, more local

³ The consequences of loading modes I, II and III for normal, in-plane shear and anti-plane shear are discussed in section 5.

dislocation activity prior to debonding. This in turn produces the dislocation shielding which allows for the large ratcheting upward effect of the practical work of adhesion. It should be added here that the continuum-based model [40] mentioned earlier was applied to this problem and for similar properties one obtains an enhancement factor of about 50 from a simulation by Beltz and co-workers [85, 86].

The second type of mesoscopic model, much more computationally intensive, is only now being aggressively implemented to understand interface separation [71–73, 86, 87]. In the latter, *ab initio* density functional theory in the multi-scale modelling scheme has been used to examine the interface energy of Al_2O_3 types and the adhesive energies of metallic films on spinel substrates. For a relatively recent review of these multi-scale models, Curtin and Miller [73] have examined this mesoscopic approach to atomistic/continuum coupling.

With various theoretical components and computational approaches described, it is appropriate to next consider the experimental approaches for measuring the work of separation.

5. Experimental measures of de-adhesion and comparisons

The emphasis here will be on linear elastic fracture mechanics (LEFM) approaches that have been developed for the assessment of interface mechanics. These generally work well because of the relatively small amount of plasticity, particular in thin films. Experimental results of these measurements will almost exclusively address metal/ceramic and metal/semiconductor interfaces where the metal is a deposited thin film. The interfacial fracture energy, or adhesion, can be qualitatively or quantitatively determined. Qualitative methods used to determine adhesion include the tape test and peel test. These tests work on a pass/fail basis. Quantitative methods, such as the scratch test, nanoindentation and the four-point bend test, calculate a value for adhesion energy, usually in units of J m^{-2} . The following will focus on metal-ceramic (oxide) interfaces and popular methods used to calculate adhesion energies.

The true work of adhesion W_{ad} , as described in equation (5), can be assumed to be equal to the Griffith [88] interfacial fracture energy. The fracture mechanics approach uses the applied strain energy release rate, G , as a means to measure the practical work of adhesion, $W_{\text{ad,P}} (G = W_{\text{ad,P}})$. When $G = W_{\text{ad,P}}$, the crack arrests; when $G < W_{\text{ad,P}}$, the crack does not grow and when $G > W_{\text{ad,P}}$ the crack grows. The practical work of adhesion takes into account the thermodynamic work ($\gamma_s + \gamma_f - \gamma_{\text{fs}}$) of the film to separate (true work of adhesion or more precisely the work of separation) and the energies dissipated by the film and substrate during separation ($D_{\text{F,S}}$) through plastic deformation [89]. The strain energy release rate, G , is more precisely an interfacial fracture energy, $G(\Psi)$, where Ψ is the phase angle of loading and is the measure of mode mixity at the crack-tip. This indicates the amount of added energy dissipation that has taken place. The mode mixity refers to the three modes of failure, opening, shearing and mixed or tearing. As defined by an expansion of equation (5), the practical work of adhesion for thin films is

$$W_{\text{ad,P}} = G(\Psi) = \gamma_f + \gamma_s - \gamma_{\text{fs}} + D_{\text{F}} + D_{\text{S}}. \quad (20)$$

The term Ψ can be defined by the loads and moment at the crack-tip [34] or the arctangent of the ratio of mode II and mode I stress intensity factors (K_{II} and K_{I} , respectively),

$$\Psi = \tan^{-1} \left(\frac{K_{\text{II}}}{K_{\text{I}}} \right). \quad (21)$$

When the phase angle of loading is 0° then the fracture energy is made of all normal forces and it is called the mode I fracture energy. When the fracture energy is made of pure shear forces the phase angle of loading is $\pm 90^\circ$; then mode II exists (figure 11). The fracture energy

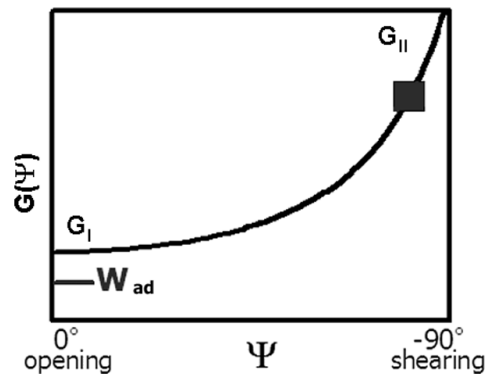


Figure 11. Fracture energy versus phase angle of loading. Square denotes approximately where $G(\Psi)$ is calculated to be on the graph. W_{ad} signifies the work of adhesion.

release rate, $G(\Psi)$, is a function of the phase angle of loading and is typically calculated to be close to the mode II fracture energy (denoted by a square in figure 11). The curve in figure 11 is the amount of energy dissipated and is higher for pure shear compared with pure opening fracture mode. The mode I fracture energy is the value which is of interest because it is made of all normal forces and is closest to the true thermodynamic work of adhesion, W_{ad} (figure 11). Because of the movement of dislocations and defects in the film, and the added energy dissipation (plasticity) of the film and substrate, the mode I energy is typically higher than W_{ad} . Three techniques for determining W_{ad} are discussed in the following.

5.1. Four-point bending

Laminated beams as a sandwich specimen provide a macroscopic test sample that incorporates a thin film into its structure. The thin film can be incorporated through many techniques, including diffusion bonding [90], which can alter the film's microstructure and interface properties, or using low temperature epoxies [91–93], which do not alter the microstructure or interface. The common sample geometry for the sandwich specimen is the four-point bend geometry, where a thin film is bonded between two rigid elastic plates and a notch is machined into the upper substrate [92–97]. The crack will propagate through the substrate and kink into the weakest interface during loading. At this point the strain energy release rate reaches a steady state, corresponding to a load plateau in the load–displacement curve. From this plateau the adhesion energy can be calculated using the sample geometry and the applied load [97]. If plasticity is constrained to the sandwiched thin film structure, only the stored elastic energy in the rigid substrates needs to be considered in order to calculate the interfacial fracture energy, G . After the interfacial crack has extended sufficiently far from the vertical pre-crack (where load plateau occurs), G is then independent of the crack length. Using beam theory, G is calculated with

$$G = \frac{21(1 - \nu^2)M^2}{4EB^2h^3}, \quad (22)$$

where M is the bending moment equal to $PL/2$, P is the load, L is the spacing between the inner and outer loading lines, B is the width of the beam, h is half the thickness and E and ν are the elastic modulus and Poisson's ratio of the bulk substrate [97].

The four-point bending technique is a good technique to use with thick films ($> 1 \mu\text{m}$) and multi-layer film stacks. However, the sandwich-type specimen tests may not account

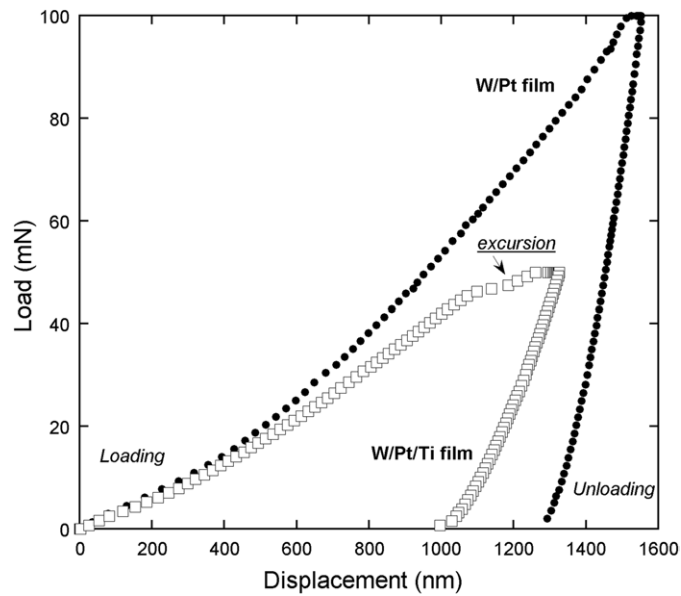


Figure 12. Load–depth curve for W/Pt and W/Pt/Ti film systems. The W/Pt/Ti film has an excursion indicating that the blister is pinned, while the W/Pt film is modelled as an unpinned blister because it has no excursion.

accurately for the residual stress of the actual film in use. Four-point bending tests also require more sample preparation than other techniques, needing samples to be cut, bonded and polished before testing can start. The technique has been used to determine the adhesion energy of copper interconnects with Ta and TaN barrier layers [98, 99], as well as low- k dielectric films and many other systems. Others have done in-depth studies on adhesion using four-point bending and should be referred to for details on the technique [92–100].

5.2. Indentation

Several groups have studied how to measure the interfacial fracture energy of films using indentation techniques [101–106]. These techniques provide a means of generating interfacial cracks on a sufficiently small scale to investigate thin film adhesion [101]. Marshall and Evans [101] have examined uniformly pre-stressed films, indented stress-free films and indented pre-stressed films with interface cracks and calculated the strain energy release for all conditions. To create a blister the total strain energy is determined by modelling the fracture as a clamped circular plate. This method assumes a rigid substrate, which makes performing this test with plastically deforming interlayers difficult. However, it can be combined with stressed overlayers, which aid in constraining the film and minimizing plasticity affects [103].

Nanoindentation can be used to initiate buckling of thin films when the film is too well adhered to the substrate by adding more energy into the system. The load–depth curves from the indentation experiments are examined for the presence of excursions. Excursions, or pop-in events, are indicative of delamination at the interface followed by through thickness film fracture. If the excursion is present then the indent is modelled as a pinned circular blister. Alternatively, if there is no excursion then the blister is considered to be unpinned (figure 12). An unpinned blister forms after the indenter tip has been removed and a pinned blister forms while the indenter tip is still in contact with the film. By measuring the height and dimensions

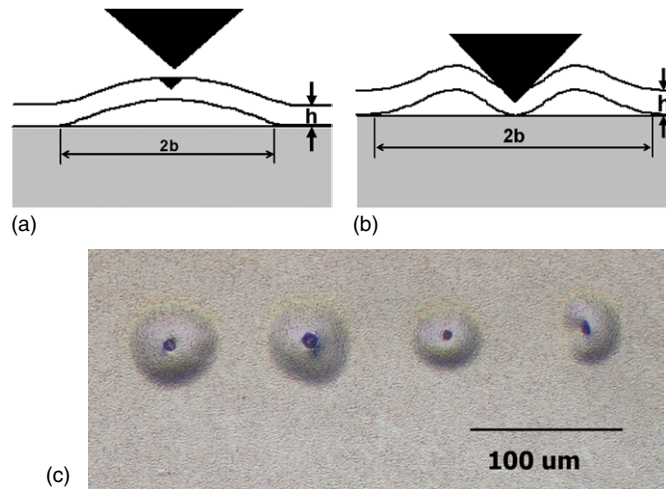


Figure 13. Schematic of the cross-sections for an unpinned (a) and pinned (b) indentation-induced blisters. (c) Optical micrograph of indentation-induced blisters.

of the blister the effective driving stress (the stress which caused a specific blister) can be determined. Figure 13 is a schematic of an unpinned and pinned indentation blister.

Nanindentation can also be coupled with acoustic emission (AE) analysis to monitor the cracking of the interface during delamination [107]. The AE signal arrives at the sensor faster than the response time of the indenter load cell during failure. The AE signal can be correlated with a position on the load–depth curve that clearly indicates if the interface cracks during the loading or unloading portion of the indentation test.

When indentation is used to induce delamination the interfacial fracture energy is calculated by modelling the delamination as a clamped circular plate, for which the strain energies are a function of the delamination radius. This allows determination of the driving force in the form of the fracture energy release rate $G(\Psi)$ [103]. For indentation-induced blisters, the fracture energy, $G(\Psi)$, takes into account the critical buckling stress, σ_b , the driving stress, σ_d , and the indentation stress, σ_1 . The combination of the different stresses generates a formula to calculate $G(\Psi)$ from

$$G(\Psi) = \frac{h\sigma_1^2(1-\nu^2)}{2E} + (1-\alpha_2)\frac{h\sigma_d^2(1-\nu)}{E} - (1-\alpha_2)\frac{h(\sigma_1-\sigma_b)^2(1-\nu)}{E}, \quad (23)$$

where α_2 is the slope of the load versus edge displacement after buckling and is given by

$$\alpha_2 = 1 - \frac{1}{1 + 0.902(1-\nu)}. \quad (24)$$

The mechanics presented above were derived by Marshall and Evans [101] who used hypothetical steps to calculate the interfacial fracture energy. Their method takes into account the residual stress in the film present after deposition and the stress caused by the indent. Kriese *et al* [103] also followed these steps and formulated a similar derivation for $G(\Psi)$ with a superlayer present. This model has a few constraints that must be noted. One assumption is that the indent remains in the film and does not penetrate the substrate, meaning the substrate is perfectly rigid. If this is assumed then all the plasticity from the indent remains in the film and causes the film to crack at the interface, thus forming a blister. This sequence of events forms an unpinned blister. DeBoer and Gerberich [105] brought up the point that even if the

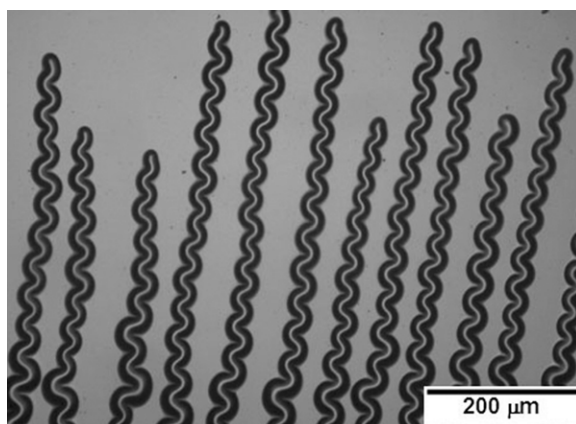


Figure 14. Example of spontaneous telephone cord buckles in a tungsten film. (Optical micrograph using Nomarski contrast.)

indent remains within the film the substrate may crack underneath the indent and not remain perfectly elastic.

The calculation of the interfacial fracture energy also depends on knowing the volume of the indent. It is assumed that the volume of the indent is conserved but this is a difficult value to calculate and is often a source of error. The volume is calculated from the tip geometry and the inelastic penetration depth. The penetration depth is determined from the extrapolation of the initial unloading slope. This is a well-established procedure because it uses the same standard procedure in nanoindentation hardness testing. Even using the same technique as with nanoindentation, the determination of the volume of the indent remains a major source of experimental variation [104].

Radial cracking around indents can also affect the calculation of the interfacial fracture energy. As it is unaccounted for in the assumptions of the models, these techniques represent a lower bound for the interfacial fracture energy [104]. It has been found that measured adhesion values greatly differ between indentation blisters with and without radial cracking [103, 108]. It is believed that radial cracking reduces the hoop stress and constraint in the film, allowing the film to curl away from the substrate [104].

5.3. Stressed overlayers

The stressed overlayer technique, first proposed by Bagchi and coworkers, was originally called the superlayer test [108, 109]. Stressed overlayer materials include tungsten [103, 111–113], chromium [104], nickel [115] and tantalum nitride [116–118]. The stressed overlayer applies a uniform stress to underlying ductile films while constraining the out-of-plane plasticity. This added energy can cause delamination by increasing the overall thickness and the total residual stress of the film. The overlayer does not react with the existing film, preserving the microstructure and structure of the interface of interest [109]. The stressed overlayer test has been used alone [111, 119], with indentation techniques [109, 112–114, 116, 117] and with tape tests [115] to successfully calculate the fracture energy release rate for several film systems including gold, copper, gold–copper, gold–chromium, platinum, platinum–titanium, titanium, and aluminium films.

Delamination of such film systems can form spontaneously. Such buckles are usually of the telephone cord morphology as seen in figure 14. These buckles are modelled as a

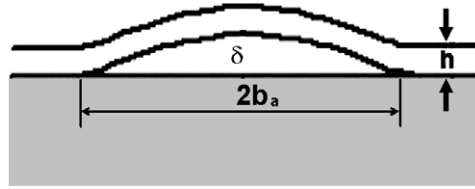


Figure 15. Schematic of the cross-section of a spontaneous buckle.

uniform width and height buckle using Hutchinson and Suo's [34] method. The dimensions of the spontaneous buckles are measured with AFM and used to calculate the stresses that arise during the buckling process. The critical buckling stress, σ_b , and the driving stress, σ_d , of the film [33] depend on the film thickness, h , the radius of the buckle, b , and the height of the buckle, δ_b (figure 15). When a stressed overlayer is used (multilayer films) the elastic modulus and Poisson's ratios are thickness-weighted using a simple rule of mixtures calculation. The critical buckling stress is the stress needed for film buckling to occur while the driving stress aids in the propagation of the delamination. For spontaneous buckles the mixed mode interfacial fracture energy, $G(\Psi)$ is calculated using

$$G(\Psi) = \left[\frac{(1 - \nu^2)h}{2E} \right] (\sigma_d - \sigma_b) (\sigma_d + 3\sigma_b). \quad (25)$$

The phase angle of loading, Ψ , is found with

$$\Psi = \tan^{-1} \left[\frac{4 \cos \omega + \sqrt{3}\xi_b \sin \omega}{-4 \sin \omega + \sqrt{3}\xi_b \cos \omega} \right], \quad (26)$$

where ω is 52.1° [120] and $\xi_b = \delta_b/h$. Equation (26) is valid for all σ_d/σ_b ratios less than 7.6. After σ_d/σ_b reaches 7.6, the spontaneous buckle phase angle is approximately equal to -90° due to the large amount of shear forces present.

The morphology that the buckle takes, especially the telephone cord (figure 14), has been the subject of much interest [120–125]. It was believed at first that anisotropy [126] was required for the telephone cord buckles to form. However, it has been shown that the telephone cord buckles can form in films under isotropic stress [127]. Another theory of the mechanism by which the telephone cord buckles form [128] examines the instability of an Euler column (straight buckle) that becomes a telephone cord buckle due to a Poisson's ratio mismatch. When Poisson's ratio for the film is greater than a critical Poisson's ratio, the edges of the straight buckle remain parallel but become wavy above a critical width value. The transition of the straight to telephone cord morphology has been found to be energetically favourable and may be the simple explanation for the frequent observations of the telephone cord buckles on thin, compressively stressed films [120, 126, 129, 130]. It is also assumed that the buckle adopts the telephone cord morphology in order to balance the driving force for delamination and the interfacial fracture energy [131].

The buckle/indentation blister dimensions can be measured using atomic force microscopy (figure 16) and are used to calculate the interfacial fracture energy or adhesion energy discussed in the previous section. Telephone cord buckles may be modelled as straight buckles, meaning that the buckle dimensions are taken at the point of inflection of the buckle. Recently, there has been a discussion on how to measure the telephone cord buckles [132] and how best to model them. Work has shown that the adhesion energy does not change between straight and telephone cord buckles modelled as straight buckles [133].

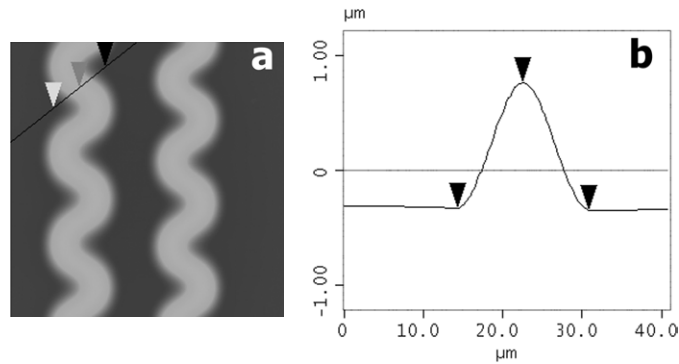


Figure 16. Example of the measuring technique used to determine the dimensions of the buckles. (a) height image from the atomic force microscope, (b) cross-section of the buckle in A.

6. Measures and comparisons

Attempts to provide a detailed understanding of what controls the work of separation of strongly adhered films are still largely novel and incomplete. This is partially due to the large number of variables that may be dependent on the chemistry and length scale [134, 135]. Consider the present understanding of thin-film adhesion in the following tabulation.

Variables	Status for deposited films
• interface chemistry termination	most often unknown but atomistic studies continue
• interface or surface reconstruction	need HREM ^a and SPM ^a
• oxidation effects	non-equilibrium
• as-deposited defect number and arrangement	generally unknown (TEM) ^a
• debonding induced dislocation arrangements	requires in situ TEM
• thickness (h) effect on plasticity	$U_p^b \propto \sigma_{ys}^2 h / E$
• thickness (h) effect on nanocrystallinity (d)	$\sigma_{ys} \propto d^{-1/2} \propto h^{-1/2}$
• effect of h and d on length scale	multiple mechanisms under study
• coupled effects of bond energy, Griffith energy and practical work of adhesion	e.g. equation (19)
• external loading mode effects	modes I, II, and III produce plasticity, dependence on interface roughness effects
• bi-material property effects on loading mode	elasticity mismatch affects mode mixity
• environmental chemistry effects	long-term thermal or concentration exposures under study

^a Transmission electron microscopy (TEM), high resolution electron microscopy (HREM) and scanning probe microscopy (SPM).

^b Plastic energy dissipation.

Of the first three sets of variables, most progress has been made using atomistic simulations as addressed above. Relatively few of these are carefully coupled to comparable experiments. For the next six which address mesoscopic phenomena and the plasticity effect, both discrete

dislocation and coupled atomistic studies are in the early stages of development. It is now generally accepted by the thin film community that plastic energy dissipation increases with $\sigma_{ys}^2 h$ since the region of plastic flow is limited to the film thickness. However, in nanocrystalline solids it is also accepted that, to first order, the Hall–Petch grain size effect would give $\sigma_{ys}^2 \sim 1/h$ since thinner films have finer-grain structures. These two effects tend to cancel. Some yield strength mechanisms give $\sigma_{ys} \sim 1/h$ which would tend to more than cancel the extent of the above plasticity effect. Finally, there are mixed-mode effects that are difficult to decouple from shear-tension coupling effects on crack-tip dislocation nucleation and multiplication, as well as fracture mode [85, 86, 136, 137]. In the following some general experimental observations are given pertinent to the above variables. This is followed by several examples of how mesoscopic modelling at the dislocation and atomistic levels are being applied to resolve a number of issues. The limitations of the various approaches representing barriers to progress will be indicated where possible.

6.1. Experimental measures

With regard to plasticity, four-point bending and the stressed overlayer methods produce the same trends. Dauskardt and Lane *et al* [91, 92, 98, 138], Wang *et al* [139] and Moody *et al* [140] have all shown that the interfacial fracture energy increases with increasing thickness. Lane *et al* [91, 92, 98, 138] and Wang *et al* [139] used four-point bending to find this result. Materials tested include Cu/TaN on SiO₂ [98] with thicknesses between 250 and 2500 nm and Ti on Al₂O₃ [139] with thicknesses greater than 1 μm . Moody *et al* [140] was able to produce similar results using tungsten stressed overlayers and various gold films on Al₂O₃. Their findings indicate a constant mixed mode fracture energy ($G(\Psi)$) for thin films less than 100 nm with increasing fracture energy for thicker films (greater than 100 nm) [140]. These results suggest that plastic energy dissipation is a large factor to consider when determining adhesion energies of ductile thin films.

Tungsten films have been delaminated from copper films of varying grain sizes to study the effect of grain size on adhesion energy [141]. The hardness properties of the copper films have also been determined through the use of continuous stiffness nanoindentation. Through the use of nanoindentation, stressed overlayers and mechanics based models the interfacial fracture energies have been calculated for these samples. A correlation exists between the hardness, and thus grain size, of a film and the interfacial fracture energy [141]. Additionally, it has been shown that a softer film requires a higher driving force for delamination, even when the delaminating film is on top of the ductile film. This was shown [141] where the grain size decreased from 1.9 to 1.1 μm resulting in an increase in the hardness from 1.2 to 1.6 GPa and a drop in the interfacial fracture energy from 2.6 to 1.4 J m⁻². Similarly, harder films show lower interfacial fracture energy due to a lack of plastic deformation compared with the plasticity of the copper film. The hardness of the film scales inversely with the region of plastic deformation around the delaminated region, demonstrating the mechanism of crack-tip plasticity dissipating energy during the delamination of a hard protective film on a softer metallic layer [141].

Environmental conditions in which these film devices operate also have a significant effect on adhesion properties. Again, using four-point bending, Lane *et al* [98, 138] found that as the moisture content of the environment increased for a given temperature range, the work of adhesion decreases. They found that the interfaces typically found in copper interconnect structures are susceptible to subcritical debonding similar to stress-corrosion cracking found in bulk glasses [98, 138]. Similarly, Cordill *et al* [142] found that prolonged environmental exposure of the gold–copper alloy film resulted in a decrease by a factor of two

in the calculated interfacial fracture energy. This drop in fracture energy, due to hydrogen embrittlement [143–147], has been observed for a number of systems, including copper [143], beryllium films [144], and nickel- and iron-based superalloys [146, 147]. In addition, Moody *et al* [145, 146] showed using a molecular dynamics calculation that hydrogen reduces the fracture stress in a nickel lattice from approximately 18 to 8 GPa at a chemical potential of -2.40 eV. These results demonstrate that environment exposure significantly reduces the interfacial fracture energy of gold conductor films with the potential to adversely affect the long-term performance and reliability of hybrid microcircuits.

The interfacial fracture energy of tungsten films on SiO_2 substrates has been calculated using spontaneous, uniform width buckles as well as indentation-induced blisters. The spontaneous buckles formed either as straight buckles or in the more energetically favourable telephone cord buckle morphology. It was found that the buckle morphology had no effect on the interfacial fracture energy value as long as the same interface was failing, such as the W– SiO_2 interface in this case. On average the interfacial fracture energy of tungsten on SiO_2 is 1.6 J m^{-2} with the phase angle of loading being -90° . Calculated values of the interfacial fracture energy for tungsten on SiO_2 ranged between 0.6 and 2.9 J m^{-2} when the indentation blisters are assumed to be pinned. Average mode I interfacial fracture energy is 0.34 J m^{-2} with spontaneous buckles and 0.37 J m^{-2} with indentation-induced blisters [148]. Using the mechanics-based models of Hutchinson and Suo [34] it has been found that these two and other techniques are complementary to one another and yield similar results for the same interface. These similarities suggest that such multiple techniques might be used as a cross-checking metric for establishing standardized measuring procedures for interfacial fracture energies of thin films [148].

6.2. Comparisons using mesoscopic modelling

Extensive interest in Cu interconnects for microelectronic applications has produced a number of theoretical approaches to line adhesion. Several of these were presented in equation (19). Three sets of data for Cu/ SiO_2 /Si were used to compare the theoretical approaches where Cu had been directly sputter deposited onto silicon wafers or evaporated onto Corning 0211 glass [109–114]. Both were considered to have Cu bonded to SiO_2 . Although the residual stress state magnitudes could have been different, they were all tensile for the initial deposit. Model comparisons were made using Griffith values for the local stress intensity factor, $k_{\text{IG}} = 0.33 \text{ MPa m}^{1/2}$, $E = 120 \text{ GPa}$, $c_{\perp} = 17 \text{ nm}$ and $n = 0.2$, the strain-hardening exponent used for the example at equation (19). For the first and the third model, two additional fitting parameters were needed, $\kappa = 10^3 \text{ MPa m}^{1/2}$ and $\alpha = 0.001$. As yield strength varies with film thickness, this was calculated from a formulation used by others [50] giving

$$\sigma_{\text{ys}}^{\text{Cu}} = \sigma_0^{\text{Cu}} [1 + \beta_{\text{Cu}} h^{-1/2}], \quad (27)$$

where σ_0^{Cu} is 400 MPa , β_{Cu} is $0.287 \mu\text{m}^{1/2}$ and h is film thickness in μm . It is seen that all G_{ψ} or practical work of adhesion data increase with increasing film thickness in figure 17(a). As the typical error bar is shown, there are real differences here due to processing conditions. It is of interest that the best fits of the exponential and power-law formulation (equations (19b) and (19c)) give almost identical solutions for this data set. For similar Cu processing conditions, an addition of 10 nm of Ti or a thin inner layer of TaN/Ta, improved the adhesion of the Cu/x/ SiO_2 interfaces [50, 89, 98, 99]. These inner layers increased W_{ad} to about 4 J m^{-2} giving $k_{\text{IG}} = 0.69 \text{ MPa m}^{1/2}$. With all other above parameters the same, comparisons with two sets of practical works of adhesion, G_{ψ} , are shown in figure 17(b). Again, both sets of adhesion data increase by more than an order of magnitude with increasing film thickness.

Also, compared with figure 17(a) with no inner layer bond, the effect of increasing the true work of adhesion to 4 J m^{-2} is to increase the practical work of adhesion by 20 to 40 J m^{-2} at the larger thicknesses. The theoretical comparisons from equations (19a) and (19b), using the dislocation shielding approach, are reasonably consistent and predictive. One could make the strain gradient plasticity model of equation (19c) fit just as well but this would require increasing the strain-hardening exponent to 0.3. It did not seem appropriate to increase this far field strain-hardening parameter in the same thickness Cu film deposit. On the other hand, is it legitimate to change the DFZ or c_{\perp} to 60 nm to obtain a reasonable fit? One can argue that the greater bond strength allowing larger local stress intensities will push the nearest dislocation further away from the crack tip. This requires c_{\perp} to increase with k_{IG} as discussed further elsewhere [50, 78, 79, 83]. As yet, however, there is no direct evidence of how the dislocation structure evolves at incipient defects in thin films undergoing de-adhesion.

Insight into the interfacial bonding aspect has been provided by Mao and Evans [149] and adapted by Tymiak *et al* [150]. They related the crack-tip plasticity to the bond strength to give

$$\sigma_{\text{bond}} = \left[\frac{8 E \mu W_{\text{ad}}}{3\pi \sigma_{\text{ys}} h} \right]^{1/2}. \quad (28)$$

Values of interfacial shear strength for Cu/Al₂O₃ and Cu/Ti/Al₂O₃ had been measured by Dehm *et al* [151] as a function of thickness. Values of W_{ad} without and with a Ti inner layer are 0.4 and 2 J m^{-2} based on Nb/Al₂O₃, Au/Al₂O₃ and Cu/Ti/SiO₂ interfaces. Along with equation (27) for yield strength, the interfacial shear strengths are predicted to first order in figure 18 from equation (28). Further development of such models await clever *ex situ* and *in situ* transmission electron microscopy experiments. Presently, these models can be considered as reasonable expressions of how the practical work of adhesion evolves with increased bonding and film thickness but not as to the specific mechanism.

Without the mechanism details, equation (19(b)) can still be semi-quantitatively used to estimate how various interfacial atomistic arrangements or chemistries might change adhesion characteristics. Assuming one knows W_{sep} from atomistic simulations and knowing that $k_{\text{IG}} = [E W_{\text{sep}}]^{1/2}$ one can show how $G_{\psi} \equiv W_{\text{ad},\rho}$ or the practical work of adhesion is changed. Keeping in mind that current theoretical simulations in figure 8 are about a factor of 2 or more greater than experimental values of W_{sep} , consider that the W_{ad} values found by Reynolds *et al* [59] were a factor of 2 greater than W_{sep} . Based on their atomistic simulations and this factor of 2, W_{sep} values for NiAl/Mo, NiAl/C/Mo and Al/S/Mo become 3.2 J m^{-2} , 2.45 J m^{-2} and 1.45 J m^{-2} , respectively. These translate to k_{IG} values of 0.8, 0.7, and $0.54\text{ MPa m}^{1/2}$. With the relationship between k_{IG}^2/E and c_{\perp} , this DFZ size can be calculated to be 100, 84 and 50 nm, respectively. Using the variation of yield strength to be similar to Cu which is appropriate for NiAl in the soft-orientation, one can use equation (27). With all of the parameters in equation (19(b)) given, G_{ψ} (same as $W_{\text{ad},\rho}$) can be determined as shown in figure 19. This zeroth order calculation is semi-quantitative but gives the scaling of how the practical work of adhesion might be dependent on both thickness and interfacial chemistry as a guide to improved multi-scale modelling.

In addition to interface chemistry, film thickness, and coupled bond energy aspects, there are external variables of loading mode, environmental chemistry and fatigue. Mode mixity and environmental effects have been discussed above but fatigue, which might be associated with thermal cycling or repeated contacts of MEMS components, has not. Bahr *et al* [152]

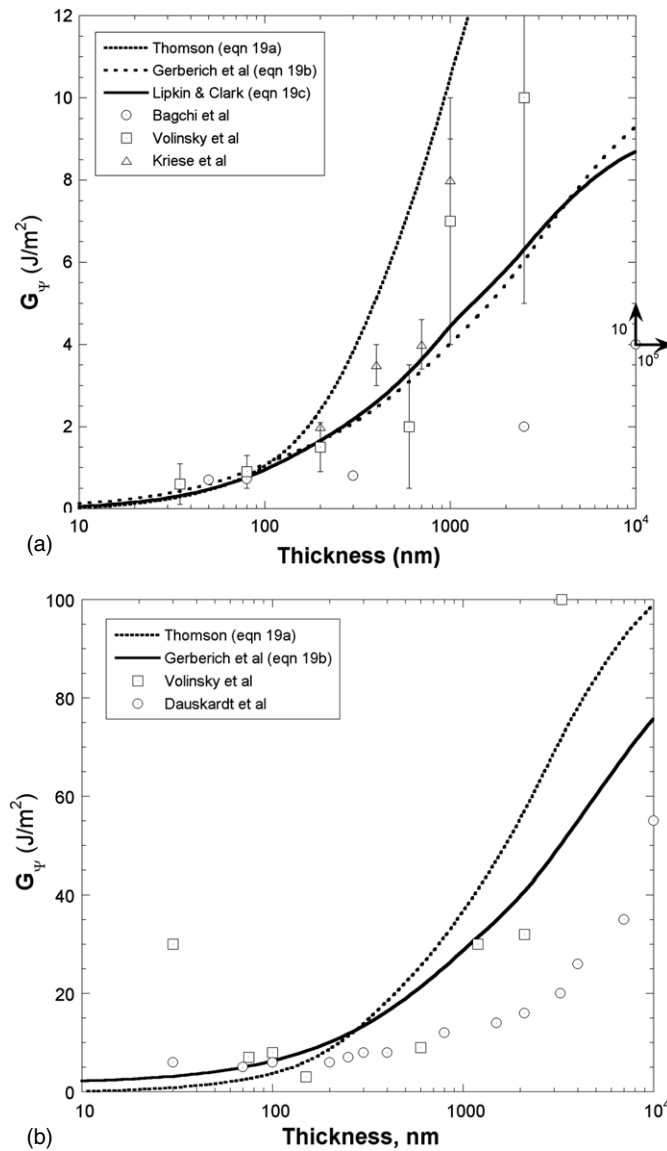


Figure 17. (a) The practical work of adhesion data increase with increasing film thickness. As the typical error bar is shown, there are real differences here due to processing conditions. Models are from equations 19(a),(b) and (c). Data are from [109–114]. (b): with all other above parameters the same, comparisons to two sets of practical works of adhesion, G_{ψ} , are shown. Again, both sets of adhesion data increase by more than an order of magnitude with increasing film thickness. Models are from equations 19(a) and (b). Data are from [50, 89, 98, 99].

conducted a study of diamond tip contacts into 1 μm thick titanium and aluminium films grown in silica glass and silicon substrates, respectively. With continuing penetration they cycled the tip with 3, 6, and 9 nm oscillations at 45 Hz. Results are shown in figure 20 and it is seen that the greater the amplitude of the oscillation, the shorter the fatigue life for crack initiation. Although they found fatigue cracks on bulk titanium that had been oxidized to obtain a 120 nm thick oxide film, such cracks were not found on the surface of the 1 μm thick films. Calculations

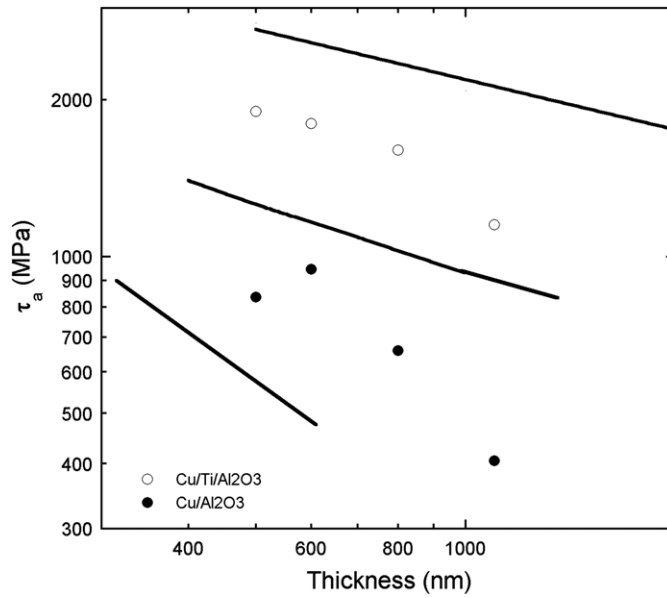


Figure 18. A log–log plot of the interfacial shear strength against the film thickness. The data demonstrates an approximately inverse relationship which suggests a dislocation pile up mechanism for interfacial yielding. The solid curves of equation (28) are represented by $\tau_a \sim \sigma_{\text{bond}}/2$.

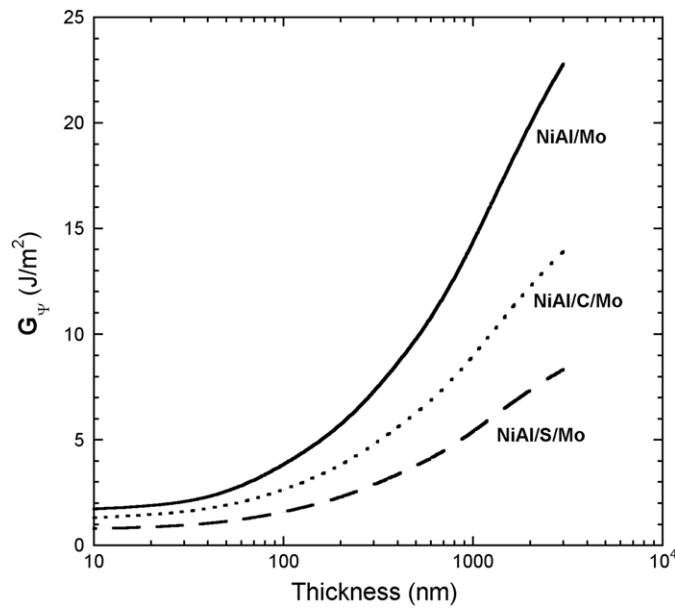


Figure 19. Using the variation of yield strength to be similar to Cu which is appropriate for NiAl in the soft-orientation, one can use equation (27). This zeroth order calculation is semi-quantitative but gives the scaling of how the practical work of adhesion might be dependent on both thickness and interfacial chemistry as a guide to improved multi-scale modelling.

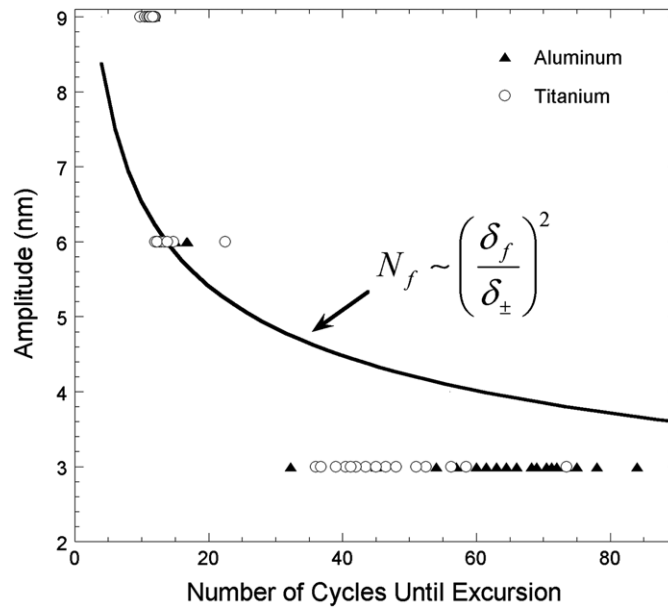


Figure 20. Relationship between the amplitude of cycling and the number of cycles until an excursion is observed [152]. It is seen that this fatigue life curve for low-cycle fatigue (equation (29)) fits the data better than might be expected.

of bond strength of these films were conducted using equation (28) resulting in a tensile bond strength of 3.8 ± 1 GPa reasonably close to the local shear stresses one might expect. For $1 \mu\text{m}$ films, the plastic zone at the contact is approaching the interface and with continued cycling cumulative damage may produce delamination. The Manson–Coffin law [153] of cumulative plastic strain damage would be appropriate in that case as given by

$$N_f \simeq \left(\frac{\varepsilon_f}{\varepsilon_{\pm}} \right)^2 \simeq \left(\frac{\delta_f}{\delta_{\pm}} \right)^2, \quad (29)$$

where ε_f is fracture ductility, ε_{\pm} is the cyclic strain, δ_f is the displacement at fracture and δ_{\pm} is the oscillation displacement. Since the strain at crack nucleation is the displacement divided by film thickness (δ_f/h) and the cyclic strain is (δ_{\pm}/h), the latter part of equation (29) results. It is seen that this fatigue life curve for low-cycle fatigue fits the data in figure 20 better than might be expected.

Whether the crack initiation in these films is near the oxide/metal surface or the metal/substrate interface is not important since for thinner films where the interface is weaker, the larger interfacial stresses will control adhesion life. Critical assessment of the above approaches suggests they are experimentally driven since such parameters as yield strength and the true work of adhesion must be measured or known *a priori* in order to correctly predict the effects of other variables. Steps toward improved understanding need to be taken for further development of more complex multi-scale models as discussed in the next section.

6.3. Comparisons using multi-scale modelling

To date there have been no truly successful comparisons of experimental de-adhesion and atomistic-based multi-scale modelling involving dislocation plasticity. This is not surprising

as a correct small-scale quantum mechanical region needs to be coupled to a larger scale million-atom region which can handle multiple dislocations and yet reproduce all of the appropriate properties in the quantum mechanics (QM) region. This large-scale, semi-empirical atomistic region then needs the appropriate handshake to a continuum region which represents large-scale elastic–plastic behaviour. Further complications arise when attempting to couple the picosecond time scale of the near field to the necessary dislocation dynamics of the mesoscale as the crack grows.

Nevertheless, there have been considerable advances toward this goal of multi-scale modelling which incorporates dislocation plasticity essential to understanding adhesion of most crystalline systems. Early on continuum-atomistic schemes were proposed in this vein which used an interatomic potential for the local region and continuum theory for the far field [71–73, 87, 154, 155]. For example, Shastry *et al* [156] used a dislocation free zone type model coupled to a hexagonal lattice array which satisfied pair-wise force laws that were modelled by the universal binding relation (UBER) of Rose *et al* [157–159]. In the same time frame an approximate method [85, 86] to account for modified unstable stacking energies, δ_{us} , was coupled to embedded atom methods (EAM). This showed that combined loading modes exist for bi-material interfaces and shear-tension coupling at the crack-tip would modify crack-tip dislocation nucleation. Later results in the time frame of 1996–1999 developed the so-called ‘quasi-continuum’ method that coupled EAM methods to large-scale discretized dislocation models [160–162]. These currently are the most highly developed methods that can handle the complexity and volume of material essential to the de-adhesion of thin metallic films. For completeness, handling large scale dislocation dynamics in the mesoscopic region is appropriate as Bulatov and Kaxiras [163, 164] and Zbib *et al* [165] have done.

Initial multi-scale modelling of much of this scheme has been applied to interface fracture of nanolaminates [166] or grain boundaries [167]. In the latter, it was found that a crack along a $\Sigma 5$ symmetrical tilt boundary would propagate a short distance intergranularly if the loading was just above the Griffith value. It would then turn after about 5 nm of growth and grow transgranularly. On the other hand if hydrogen impurities were introduced, it would grow intergranularly with no deflection since $k_{IG}^{Fe-H} < k_{IG}^{Fe}$. This is consistent with both experiments on iron and steels [68] as well as the semi-quantitative approach illustrated for NiAl/Mo and NiAl/S/Mo in figure 19, with k_{IG} being lowered by sulfur at the interface boundary. One illustration regarding the quasi-continuum method of Tadmor and co-workers [154–162] is illustrated in figure 21. With a total of 8×10^6 atoms but a computational mesh of only 1.5×10^4 representative atoms, they simulated a crack interacting with dislocations emanating from a $\Sigma 21(421)$ tilt boundary in aluminium. As the crack approached the grain boundary, as illustrated in figure 21, dislocations were emitted from the tilt boundary at $t = 0$. With increasing load and time, more dislocations are emitted resulting in crack-tip blunting from about a 2.5 to a 10.5 Å radius as it arrests at the grain boundary. Using the same approach, however, they show that a similar crack approaching a $\Sigma 5(\bar{1}20)$ tilt boundary produced no dislocation emission and hence no crack-tip shielding.

As yet, none of these approaches have been coupled to experiments where similar length scales have been involved. Silicon would be an excellent choice as both dislocation emission and crack-tip/dislocation arrangements and shielding can be studied due to the low line defect densities. Unfortunately, existing Stillinger–Weber [169] and Tersoff [170] atomistic potentials are inadequate as the former predicts an incorrect fracture mode and the latter gives a non-physical crack-tip structural arrangement. A couple of additional cautions are in order here as these multi-scale models are in their early development stages. Hugo *et al* [171] have shown through *in situ* studies of 100 nm thick Ni films deposited by either DC magnetron sputtering or laser deposition that dislocation nucleation and motion occurs in nanocrystalline grains as small

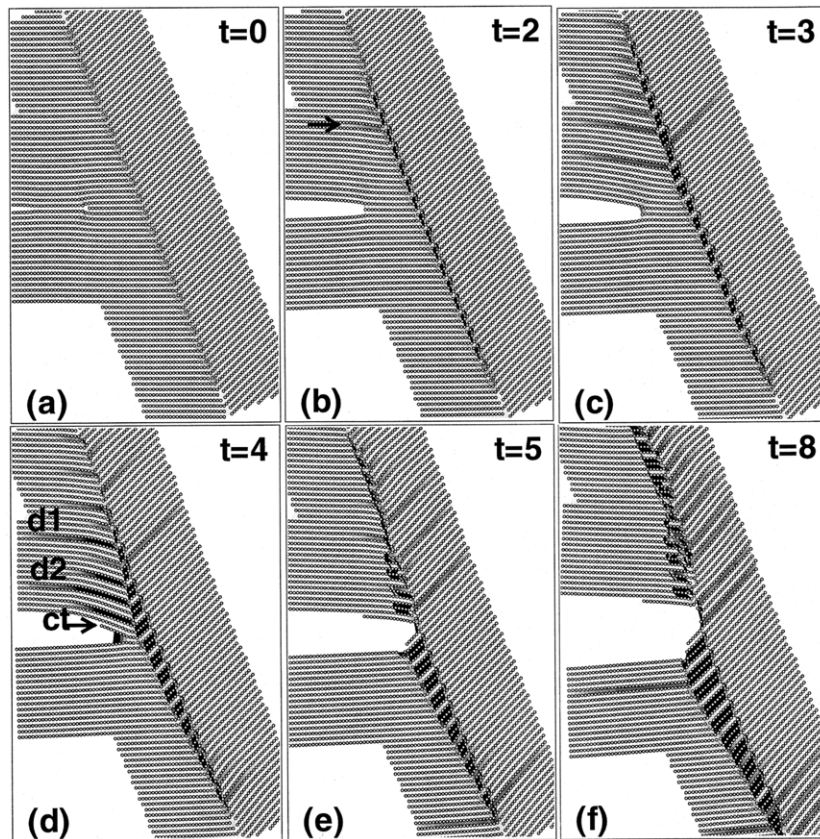


Figure 21. Time sequence of a quasi-continuum simulation of a crack approaching a tilt boundary in aluminium. After Miller *et al* [168].

as 10 nm at a pre-existing crack. This gives considerable credibility to the semi-quantitative mesoscopic models developed thus far and anticipated multi-scale models applicable to thin-film de-adhesion. However, Kumar *et al* [172] report that crack-tip dislocations in nanocrystalline nickel can be full burgers vector dislocations, and not extended partials, as predicted by simulations. Whether this is due to unique experimental conditions of thin film transmission electron microscopy or the time and temperature scale problems of atomistic simulations has yet to be sorted out. It is an additional caution then that multi-scale modelling needs to have atomistic potentials appropriately coupled to schemes which can handle the type of length, time and temperature scales being simulated.

Finally, all the multi-scale modelling schemes that have been discussed here using molecular dynamics are atomistic potentials most applicable to metallic systems. As Pettifor [173] points out, however, an atom-based potential is not as useful for covalently-bonded systems as a bond-based potential. The latter relates the attractive bond energy to both σ and π bonding giving

$$U_{\text{bond}} = \sum_{i \neq j} [\beta_{\sigma}(R_{ij}) \Theta_{\sigma}^{ij} + \beta_{\pi}(R_{ij}) \Theta_{\pi}^{ij}]. \quad (30)$$

Here, β_{σ} and β_{π} are integrals where R_{ij} are bond lengths and Θ are σ and π bond orders. The latter are dependent on the local environment about a given ij bond. At more complex

interfaces involving covalent bonding then, such problems need to be solved for appropriate atomistic potentials used in such multi-scale modelling schemes.

To summarize this brief section, three quite different reviews applicable to future developments in understanding adhesion physics involving plasticity are highly recommended. The first by Pettifor [173] reviews materials modelling from a physicist's viewpoint, and is hierarchical in concept. The second by Li *et al* [174] reviews atomistic modelling of mechanical behaviour from the viewpoint of a materials scientist. From a mechanics viewpoint, Curtin and Miller [175] emphasize the multi-scale modelling approach that is viewed as being complementary to hierarchical approaches.

7. Summary and perspective

Adhesion physics is affected by a wide range of forces and corresponding stresses resulting from the many types of bonding, interfacial chemistries and complex loading conditions. The latter depends on external combinations of normal and shear stresses as well as bi-material characteristics. In turn these determine the magnitude of line defect evolution which further increases the practical work of adhesion in crystalline solids. Parallel efforts using atomic force microscopy (AFM)-based instruments, large-scale computational materials science and condensed matter physics are beginning to evolve. This will be required to understand complex adhesion phenomena central to the appropriate description of friction and wear.

Described herein are some of the phenomena, the magnitudes and differences between the true work of adhesion, the work of separation and the practical work of adhesion. In terms of emphasis, metal/ceramic and metal/semiconductor systems are emphasized with a shorter review of adhesive organic contacts. The future is promising wherein a connectivity of length, time and temperature scales between experiment and simulation will be realized. This requires a parallel development of atomistic checks and balances as in hierarchical versus multi-scale modelling to be sure that the less precise but more expansive molecular dynamics schemes can reproduce the specifics of near field as well as connectivity to the far field. Similarly, on the experimental side most studies have been hierarchical in nature and few have considered examining the physics of adhesion across the length, time and temperature scales now becoming available to AFM and nanoindentation instruments. Neither of these approaches, however, will be sufficient without appropriate multi-scale modelling which will integrate the picture for complex engineering problems.

Acknowledgments

The authors are grateful to N R Moody of Sandia National Laboratories for his review and helpful comments. W A Curtin of Brown University and K Sieradski of Arizona State University are also thanked for the many technical discussions and helpful comments. Finally, the authors would like to thank C B Carter and S L Girshick of the University of Minnesota for assistance and participation in grants from NSF (Grant No DGE-0114372), NIRT (Grant No DMI0103619) and DOE (Grant No DE-AC04-94AL85000).

Appendix A. Pull-off forces for clean metal contacts

Pethica and Tabor's study [25] demonstrated that the resistivity of an indentation contact during unloading and just prior to de-adhesion stayed nearly the same. This would mean that the contact area up to the point of de-adhesion also remained constant. It is clear that their

contacts had produced plastic flow [26]. For spherical contacts, Johnson's spherical cavity model gives the flow stress, σ_f , to be one-third the mean pressure or hardness, giving

$$\sigma_f^{(-)} = \frac{F_c}{3\pi a^2}. \quad (\text{A1})$$

During pull-off

$$\sigma_f^{(+)} = \frac{F_{ad}}{\pi a_{ad}^2}, \quad (\text{A2})$$

where πa_{ad}^2 is the contact area at pull-off. For ductile fracture of a non-hardening material, if fully bonded and there is no Bauschinger effect, these two flow stresses should be equal. Setting these equal and invoking the experimental finding of equation (2) in the main text to eliminate F_c results in

$$F_{ad} = \sqrt{3}\beta^3 \left(\frac{a}{a_{ad}}\right)^4. \quad (\text{A3})$$

One can see in figure 3 that for their experimental data with $\beta = 1.5 \mu\text{N}^{1/3}$ that $a = a_{ad}$ for F_{ad} equal to $6 \mu\text{N}$ whereas $a \sim 2a_{ad}$ for F_{ad} equal to $94 \mu\text{N}$. This just about spans the adhesion force range in their data and suggests some small crack extension prior to pull-off at the largest forces.

Appendix B. Effect of interfacial dislocations on the work of adhesion

A nanoindentation-induced blister, similar to that shown in figure 13(c) has resulted from delamination of a 500 nm thick film. For this example, the following properties and loading conditions are assumed in conjunction with the schematic of figure 9:

$$\begin{aligned} E &= 250 \text{ GPa}; & \mu &= 100 \text{ GPa}; & \sigma_{ys} &= 1 \text{ GPa} \\ G_{ad} &= 4 \text{ J m}^{-2}; & b &= 0.25 \text{ nm}; & t &= 500 \text{ nm} \\ P &= 1 \text{ mN}; & R_{tip} &= 1 \mu\text{m}; & \delta &= 200 \text{ nm}; & b_a &= 10 \mu\text{m} \end{aligned}$$

The loading conditions are a conical diamond tip with a $1 \mu\text{m}$ radius being driven 200 nm into a 500 nm thin film by a 1 mN load. This has produced a $10 \mu\text{m}$ radius blister, b_a , at arrest.

Crack initiation. The loading conditions for crack initiation are taken from some similar experimental observations. Consider that 400 dislocations ($\delta/2b$) could be created if half of the indenter displacement was inelastic and these resided at the interface. They would be spread over a plastic zone of radius, C , given in terms of the compressive load, P , and yield strength, σ_{ys} , by

$$C \simeq \left(\frac{3P}{2\pi\sigma_{ys}}\right)^{1/2} \simeq 1.2 \mu\text{m} \quad (\text{A4})$$

using a continuum estimate [27]. The contact radius from a $1 \mu\text{m}$ radius loading tip with $a \simeq (2\delta R)^{1/2}$ is $0.6 \mu\text{m}$, half the plastic zone. Using $0.9 \mu\text{m}$ as an average concentric prismatic loop punched out one can calculate a dislocation density at the indenter based upon line length per unit volume from

$$\rho_i = \frac{2\pi\bar{a}N}{\pi C^2 t} = 10^{15} \text{ m}^{-2}. \quad (\text{A5})$$

With an average concentric loop radius of $\bar{a} \sim (C+a)/2$, one can determine a dislocation energy of

$$W_{\perp} \approx \rho \frac{\mu b^2}{4\pi} 2\pi\bar{a} \approx 1.88 \text{ J m}^{-2}. \quad (\text{A6})$$

It is seen that this is a substantial portion of the ‘measured’ strain energy release rate of 4 J m^{-2} for this 500 nm thick film. However, this is at initiation and not at arrest where measurements are made.

Crack arrest. For this thin film, plane stress is assumed with the knowledge that a plane strain calculation gives a similar result. One can use a fracture mechanics approach here with a mixed mode stress intensity, K_ψ , given by $\{EG_\psi\}^{1/2}$ to be $1 \text{ MPa m}^{1/2}$. This can then be used to estimate the crack-tip plastic zone in which dislocations would be distributed at arrest from

$$R_p \approx K_\psi^2 / \pi \sigma_{ys}^2 \approx 300 \text{ nm}. \quad (\text{A7})$$

To estimate crack-tip emitted dislocations assumed to remain at the interface, the crack-tip displacement, δ_c , is used giving

$$N = \delta_{\text{tip}} / b = \frac{K_\psi^2}{\sigma_{ys} E b} = 16. \quad (\text{A8})$$

While there are many fewer dislocations here, they are much longer being located along the periphery of the blister. As typical of many experiments, the blister is assumed to be $10 \mu\text{m}$. Using line length per unit volume, one can calculate the dislocation density at the crack tip from using (A8) for N to give

$$\rho_c = \frac{2\pi b_a N}{\pi [b_a^2 - (b_a - R_p)^2] t} = 1.08 \times 10^{14} \text{ m}^{-2} \quad (\text{A9})$$

Analogous to equation (A6), the dislocation energy becomes

$$W_\perp \simeq \rho_c \frac{\mu b^2}{4\pi} 2\pi b_a \simeq 3.38 \text{ J m}^{-2} \quad (\text{A10})$$

Again, this dislocation energy would have a substantial effect on the measured work of separation if all dislocations were tip-emitted and these remained at the interface. It is noted that these crack-tip-emitted dislocations, although fewer, could have a greater effect on the adhesion energy as they have greater line length.

Appendix C. Crack-tip dislocation emission and shielding

Emission criteria arose out of an experimental need to explain the brittle to ductile transition (BDT) and later out of a more theoretical nature to resolve the Rice paradox. This was explained and resolved by the seminal Rice–Thomson [175] paper which gave the BDT in terms of a core cut-off criterion. A brief description here should suffice.

As an example, consider a typical thin film delamination where G might be 0.8 J m^{-2} representing a K_{III} of $0.4 \text{ MPa m}^{1/2}$ for a 100 GPa shear modulus material. Note that for illustrative purposes the mode III is used here whereas most thin film situations are largely mode I and II. For a very thin film there are two solutions for the equilibrium of forces. These forces are from the applied stress intensity K_{III} , the image force trying to drag the dislocation back to the free surface, $\mu b / 4\pi r$, and the lattice friction stress, σ_f . This force balance is given by Masuda-Jindo *et al* [176], and Thomson [74, 75].

$$\frac{K_{\text{III}}}{\sqrt{2\pi r}} - \frac{\mu b}{4\pi r} - \sigma_f = 0. \quad (\text{A11})$$

At a typical value of the friction stress of 500 MPa, there are two values of the equilibrium of forces where the system is at rest, i.e. $\Sigma F = 0$. This is illustrated in figure A1. Here we see that the positive applied shear stress, σ_{yz}^+ times the Burger’s vector, b , would drive a nucleated

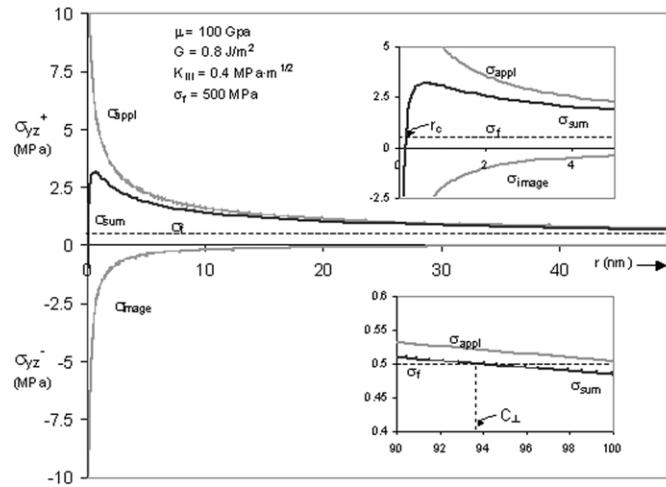


Figure A1. Representation of crack-tip emission and arrest as a balance between the applied K_1 stress field, the free surface image force and the friction of equation (A11).

dislocation away from the crack tip. Alternatively, the image force of $\sigma_{yz}^- b$ would pull the dislocation toward the crack tip. Clearly, for $r < r_c$ the image force would attract the emitted dislocation back into the crack. However, since there is a lattice resistance, σ_f , the applied stress from the crack together with the image force must exceed the friction stress before it can glide further. This is achieved at r_c . Once the local stress exceeds σ_f it can spontaneously glide from r_c to c_\perp before it arrests. It is seen that at c_\perp the net shear stress can no longer provide a force to exceed lattice friction. For a single dislocation emitted under increasing applied stress intensity of this example, the dislocation could freely travel from the core cut-off at 0.168 nm where it exceeds r_c to the dislocation free zone at $r = 94 \text{ nm} = c_\perp$. For the second dislocation emitted there would be the simple equilibrium of equation (17) plus the interactive force of the previous dislocation. The added complexity of dislocation–dislocation interactions (Atkinson and Clements [76]) result in an interaction of forces shown below.

The complete procedure for forming the constitutive equations of an anisotropic dislocation shielding model and a few preliminary calculations can be found elsewhere (Atkinson and Clements [76], Lii *et al* [78, 79]). Only part of the solution is indicated here. Presented are four major stress sources and their equations: the stress due to the dislocations interacting with each other, σ'_{kl} , the stress due to the interaction of the crack and all the dislocation, σ''_{kl} , the interactions of the external stress and the crack, σ'''_{kl} , and the external applied stress, T_{kl} . Hence, the stress tensor can be expressed as

$$\sigma_{kl} = \sigma'_{kl} + \sigma''_{kl} + \sigma'''_{kl} + T_{kl}, \quad k = 1, 2, 3 \quad \ell = 1, 2 \quad (\text{A12})$$

$$\sigma'_{kl} = \frac{(-1)^\ell}{2\pi} \text{Re} \left\{ \sum_I \sum_\alpha \left[L_{k\alpha} M_{\alpha j} P_\alpha^{2-\ell} \frac{d_j^{(I)}}{Z_\alpha - K_a^{(I)}} \right] \right\}$$

$$\sigma''_{kl} = \frac{(-1)^{\ell-1}}{4\pi} \text{Re} \left(\sum_I \sum_\alpha \sum_\beta L_{k\alpha} M_{\alpha j} P_\alpha^{2-\ell} \frac{d_j^{(I)}}{(Z_\alpha^2 - 1)^{1/2}} \right. \\ \left. \times \left[L_{j\beta} M_{\beta i} \left[\frac{(Z_\alpha^2 - 1)^{1/2} - (K_\beta^{(I)^2} - 1)^{1/2}}{(Z_\alpha - K_\beta^{(I)})} - 1 \right] \right] \right)$$

$$\begin{aligned}
& + \bar{L}_{j\beta} \bar{M}_{\beta i} \left[\frac{(Z_\alpha^2 - 1)^{1/2} - (\bar{K}_\beta^{(I)})^2 - 1)^{1/2}}{Z_\alpha - \bar{K}_\beta^{(I)}} - 1 \right] \Bigg) \Bigg) \\
\sigma_{kl}''' &= -\text{Re} \left\{ \sum_\alpha L_{k\alpha} M_{\alpha j} P_\alpha \left[\frac{Z_\alpha}{(Z_\alpha^2 - 1)^{1/2}} - 1 \right] T_{j2} \right\} \\
\sigma_{kl}''' &= \text{Re} \left\{ \sum_\alpha \left[L_{k\alpha} M_{\alpha j} \frac{Z_\alpha}{(Z_\alpha^2 - 1)^{1/2}} \right] T_{j2} \right\} - T_{k2}.
\end{aligned}$$

Here Re denotes the real part, K_α denotes the positions of dislocations, Z_α is the generic point where the stress state is evaluated and T_{22} is the only non-zero applied stress for uniaxial tension considered for this type of simulation. Also, $d_j^{(I)}$ is related to the Burgers vector of magnitude $b_i^{(I)}$

$$b_i^{(I)} = B_{ij} d_j^{(I)} \quad (\text{A13})$$

and the matrices \mathbf{B} , \mathbf{L} , \mathbf{M} and \mathbf{P} are functions of the elastic constants. In the computation, presented elsewhere [76, 77] the sample material was iron for which the elastic constants are $C_{11} = 24.2$, $C_{12} = 14.65$ and $C_{44} = 11.2$ in units of 10^4 MPa. Certain restrictions were considered in performing the simulations. For instance, the friction stress should be relatively uniform over the sample material since it is one of its intrinsic properties. The total shear stress acting on the dislocations in their slip plane and specified slip plane and specified slip direction must be equal to the intrinsic resistance. This condition is given by

$$\sigma_{\text{fric}} = \sigma_{kl} n_k b_l, \quad (\text{A14})$$

where σ_{kl} is the stress tensor specified in equation. (A12), n_k is the slip plane normal, and b_i is the slip direction.

Such simulations, both static and dynamic, have now been replaced by multi-scale modelling schemes which can take all force interactions into account as well as coupling discretized dislocation regimes to the necessary quantum mechanics description of bond separation.

References

- [1] <http://www.engr.sjsu.edu/cgi-bin/cme/mate/mate.cgi?read=360>
- [2] Dedkov G V 2000 Experimental and theoretical aspects of the modern nanotribology *Phys. Status Solidi a* **179** 3–75
- [3] Bowden F P and Bastow S H 1932 Contact of smooth surfaces *Nature* **129** 437–8
- [4] Bowden F P and Leben L 1938 Nature of sliding and the analysis of friction *Nature* **141** 691–2
- [5] Moore A J W, Tabor D and Bowden F P 1943 The ploughing and adhesion of sliding metals *J. Appl. Phys.* **14** 80–91
- [6] Maugis D and Pollock H M 1981 Surface forces and adherence at metal microcontacts *Acta Metall.* **32** 1323–34
- [7] Binnig G, Quate C F and Gerber C 1986 Atomic force microscopy *Phys. Rev. Lett.* **56** 930–3
- [8] Johnson K L, Kendall K and Roberts A D 1971 *Proc. R. Soc. Lond. A* **324** 301–13
- [9] Derjaguin B V, Muller V N and Toporov Y P 1975 *J. Colloid Interface. Sci.* **53** 314–26
- [10] Hui C Y, Baney J M and Kramer E J 1998 *Langmuir* **14** 6570–8
- [11] Chaffin K A, Knutsen J S, Brant P and Bates F S 2000 High-strength welds in metallocene polypropylene/polyethylene laminates *Science* **288** 2187–99
- [12] Mesarovic S D and Johnson K L 2000 Adhesive contact of elastic–plastic spheres *J. Mech. Phys. Solids* **48** 2009–33
- [13] Sheng X, Jung T, Wesson J A and Ward M D 2005 Adhesion at calcium oxalate crystal surfaces and the effect of urinary constituents *Proc. Natl. Acad. Sci. USA* **11** 267–72

- [14] Garif Y S, Gerberich W W and Pocius A V 2004 Thermally activated parameters of self-adhesion in acrylic pressure sensitive-like networks *J. Adhes.* **80** 61–85
- [15] Moody N R, Huang R Q, Venkataraman S, Angelo J E and Gerberich W W 1998 Adhesion and fracture of tantalum nitride films *Acta Mater.* **46** 585–97
- [16] Israelachvili J N 1991 *Intermolecular and Surface Forces* 2nd edn (London: Academic)
- [17] Maugis D 2000 *Contact, Adhesion, and Rupture of Elastic Solids* (New York: Springer) pp 307–11
- [18] Israelachvili J N 2005 Importance of pico-scale topography of surfaces for adhesion, friction and failure *MRS Bull.* **30** 533–9
- [19] Drelich J 2002 Scanning probe microscopy (SPM) in interfacial phenomena *J. Adhes. Sci. Technol.* **16** 749–998
- [19] Drelich J 2005 Scanning probe microscopy (SPM) in interfacial phenomena *J. Adhes. Sci. Technol.* **19** 146–405 (guest editor)
- [20] Grierson D S, Flater F E and Carpick R W 2005 Accounting for the JKR-DMT transition in adhesion and friction measurements with atomic force microscopy *J. Adhes. Sci. Technol.* **19** 291–301
- [21] Attard P 2005 Friction, adhesion and deformation: dynamic measurements with the atomic force microscope *J. Adhes. Sci. Technol.* **16** 753–91
- [22] Wahl K J, Asif S A A, Greenwood J A and Johnson K L 2006 Oscillating adhesive contacts between micron-scale tips and compliant polymers *J. Colloid Interface Sci.* **296** 178–88
- [23] Leite F L and Herrmann P S P 2005 Application of atomic force spectroscopy (AFS) to studies of adhesion phenomena: a review *J. Adhes. Sci. Technol.* **19** 365–405
- [24] Vezenov D V, Noy A and Ashby P 2005 Chemical force microscopy: probing chemical origin of interfacial forces and adhesion *J. Adhes. Sci. Technol.* **19** 313–64
- [25] Pethica J B and Tabor D 1979 Contact of characterized metal surfaces at very low loads: deformation and adhesion *Surf. Sci.* **89** 182–90
- [26] Salmeron M, Folch A, Neubaauer G, Tomitori M and Ogletree D F 1992 Nanometer scale mechanical properties of Au(111) thin films *Langmuir* **8** 2832–42
- [27] Johnson K L 1985 *Contact Mechanics* (Cambridge: Cambridge University Press)
- [28] Gerberich W W, Mook W M, Perrey C R, Carter C B, Baskes M J, Murkerjee R, Gidwani A, Heberlein J, McMurray P H and Girschick S L 2003 Superhard silicon nanospheres *J. Mech. Phys. Solids* **51** 979–92
- [29] Mook W M, Jungk J M, Cordill M J, Moody N R, Sun Y, Xia Y and Gerberich W W 2003 Geometry and surface state effects on the mechanical response of Au nanostructures *Z. Metallk.* **95** 979–92
- [30] Gerberich W W, Cordill M J, Mook W M, Moody N R, Perrey C R, Carter C B, Mukherjee R and Girschick S L 2005 A boundary constraint energy balance criterion for small volume deformation *Acta Mater.* **53** 2215–29
- [31] Eshelby J D, Frank F C and Nabarro F R N 1951 The equilibrium of linear arrays of dislocation *Phil. Mag.* **42** 351–64
- [32] Cordill M J *et al* 2005 Plasticity responses in ultra-small confined cubes and films *Acta Mater.* accepted
- [33] Fowkes F W 1963 Additivity of intermolecular at interfaces. I. Determination of the contribution to surface and interfacial tensions of dispersion forces in various liquids *J. Phys. Chem.* **67** 2538–41
- [34] Hutchinson J W and Suo Z 1992 Mixed mode cracking in layered materials *Adv. Appl. Mech.* **29** 64–191
- [35] Huang H and Gerberich W W 1994 Quasi-equilibrium modelling of the toughness transition during semi-brittle cleavage *Acta Metall. Mater.* **42** 639–47
- [36] Johnson K L 1999 Mechanics of adhesion *Tribol. Int.* **31** 413–18
- [37] Carpick R W, Ogletree D F and Salmeron M 1999 *J. Colloid Interface Sci.* **211** 395–400
- [38] Biggs S and Spinks G 1998 Atomic force microscopy investigation of the adhesion between a single polymer sphere and a flat surface *J. Adhes. Sci. Technol.* **12** 461–78
- [39] Rice J R 1988 Elastic fracture mechanics concepts of interfacial cracks *J. Appl. Mech.* **55** 98–103
- [40] Tvergaard V and Hutchinson J W 1993 The Influence of plasticity on mixed mode interface toughness *J. Mech. Phys. Solids* **41** 1119–35
- [41] Suo Z, Shih C F and Varias A G 1993 A theory for cleavage cracking in the presence of plastic flow *Acta Metall. Mater.* **41** 1551–7
- [42] Ellsner G, Korn D and Rühle M 1994 The influence of interface impurities on fracture energy of UHV diffusion bonded metal-ceramic bicrystals *Scr. Metall. Mater.* **31** 1037–42
- [43] Wang H R, Gerberich W W and Skowronek C J 1993 Fracture mechanics of Ti/Al₂O₃ interfaces *Acta Metall. Mater.* **41** 2425–32
- [44] Venkataraman S K, Kohlstedt D L and Gerberich W W 1993 Metal-ceramic interfacial fracture resistance using the continuous microscratch technique *Thin Solid Films* **223** 269–75
- [45] Needleman A 1987 A continuum model for void nucleation by inclusion debonding *J. Appl. Mech.* **54** 525–31
- [46] Huang Y, Zhang L, Guo T F and Hwang K C 1995 Near-tip fields for cracks in materials with strain-gradient effects *Proc. IUTAM Symp. Nonlinear Analysis* ed J R Willis (Cambridge: Kluwer) pp 231–42

- [47] Lipkin D M, Clarke D R and Beltz G E 1996 A strain-gradient plasticity model of cleavage fracture in plastically deforming materials *Acta Mater.* **44** 4051–8
- [48] Jiang H, Huang Y, Zhuang Z and Hwang K C 2001 Fracture in mechanism-based strain gradient plasticity *J. Mech. Phys. Solids* **49** 979–93
- [49] Huang Y, Gao H and Hwang K C 1999 Strain-gradient plasticity at the micron scale *Progress in Mechanical Behavior of Materials Proceedings of ICM-8* vol III, ed F Ellyin and J W Provan, (Victoria, BC: Fleming) pp 1051–6
- [50] Volinsky A A, Moody N R and Gerberich W W 2002 Interfacial toughness measurements for thin films on substrates *Acta Mater.* **50** 441–6
- [51] Becker R 1938 Nucleus formation in the separation of metallic mixed crystals *Ann. Phys.* **32** 128–40
- [52] Lee Y W and Aaronson H I 1980 Anisotropy of coherent interphase boundary energy *Acta Metall.* **28** 539–48
- [53] Borchers C and Bormann R 2005 Determination of low-temperature interfacial energies from a pair interaction model *Acta Mater.* **53** 3695–701
- [54] Finnis M W 1996 The theory of metal-ceramic interfaces *J. Phys.: Condens. Matter.* **8** 5811–36
- [55] Batyrev I G, Alavi A and Finnis M W 2000 Equilibrium and adhesion of Nb/sapphire: The effect of oxygen partial pressure *Phys. Rev. B* **62** 468–4706
- [56] Bennet I J, Kranenburg J M and Sloof W G 2005 Modeling the influence of reactive elements on the work of adhesion between oxides and metal alloys *J. Am. Ceram. Soc.* **88** 2209–16
- [57] Siegel D J, Hector L G Jr and Adams J B 2002 Adhesion, stability and bonding at metal/metal-carbide interfaces: Al/WC *Surf. Sci.* **498** 321–36
- [58] Siegel D J, Hector L G Jr and Adams J B 2002 First-principles study of metal-carbide/nitride adhesion: Al/VC vs. Al/VN *Acta Mater.* **50** 619–31
- [59] Reynolds J E, Roddick R E, Smith J R and Srolovitz D J 1999 Impurity effects on adhesion at an interface between NiAl and Mo *Acta Mater.* **47** 3281–9
- [60] Lipkin D M, Israelachvili J N and Clarke D R 1997 Estimating the metal-ceramic van der waals adhesion energy *Phil. Mag. A* **76** 715–28
- [61] Evans A G, Hutchinson J W and Wei Y 1999 Interface adhesion: Effects of plasticity and segregation *Acta Mater.* **47** 4093–113
- [62] Ji H, Was G S and Thouless M D 1998 Determination of the fracture toughness of the niobium/sapphire interface *Mater. Res. Soc. Symp.* vol 522, ed N R Moody *et al* (Warrendale, PA: Materials Research Society) 325–31
- [63] Schönberger U, Andersen O K and Methfessel M 1992 Bonding at metal-ceramic interfaces; ab initio density-functional calculations for Ti and Ag on MgO *Acta Metall. Mater.* **40** S1–10
- [64] Gumbsch P, Daw M S, Foiles S M and Fischmeister H F 1991 Accommodation of the lattice mismatch in a Ag/Ni heterophase boundary *Phys. Rev. B* **43** 113833–7
- [65] Van Swygenhoven, Spaczer H M and Caro A 1999 Microscopic description of plasticity in computer generated metallic nanophase samples: a comparison between Cu and Ni *Acta Mater.* **47** 3117–26
- [66] Yamakov V, Wolf D, Salazar M, Phillpot S R and Gleiter H 2001 Length-scale effects in the nucleation of extended dislocations in nanocrystalline Al by molecular-dynamics simulation *Acta Mater.* **49** 2718–22
- [67] Hoagland R G, Kurtz R J and Henager C H Jr 2004 Slip resistance of interfaces and the strength of metallic multilayer composites *Scr. Mater.* **50** 775–9
- [68] Gerberich W W, Oriani R A, Lii M J, Chen X and Foeke T 1991 The necessity of both plasticity and brittleness in the fracture thresholds of iron *Phil. Mag. A* **63** 363–76
- [69] Hirsch P B, Roberts S G and Samuels J 1987 The dynamics of dislocation generation at crack-tips and the ductile-brittle transition *Scr. Metall.* **21** 11523–8
- [70] Voronoi G J 1908 *Reine Angew. Math.* **134** 198
- [71] Tadmor E B, Ortiz M and Phillips R 1996 Quasicontinuum analysis of defects in solids *Phil. Mag. A* **73** 1529–63
- [72] Miller R, Tadmor E B, Phillips R and Ortiz M 1998 Quasicontinuum simulation of fracture at the atomic scale *Modelling Simul. Mater. Sci. Eng.* **6** 607–38
- [73] Curtin W A and Miller R E 2003 Atomistic/continuum coupling in computational materials science *Modelling Simul. Mater. Sci. Eng.* **11** R33–68
- [74] Thomson R 1986 Physics of fracture *Solid State Phys.* **39** 1–129
- [75] Thomson R M 1987 Physics of fracture *J. Phys. Chem. Solids* **48** 965–83
- [76] Atkinson C and Clements D L 1973 The influence of anisotropy and crystalline slip on relaxation at a crack tip *Acta Metall.* **21** 55–60
- [77] Lii M J and Gerberich W W 1988 The stress state close to a crack tip shielded by a dislocation array *Scr. Metall.* **22** 1779–82
- [78] Lii M J 1989 *PhD Thesis* University of Minnesota, Minneapolis

- [79] Lii M J, Chen X F, Katz Y and Gerberich W W 1990 Dislocation modelling and acoustic emission observation of alternating ductile/brittle events in Fe 3 wt.% Si crystals *Acta Metall. Mater.* **38** 2435–53
- [80] Hsia K J, Suo Z and Yang W 1994 Cleavage due to dislocation confinement in layered materials *J. Mech. Phys. Solids* **42** 877–96
- [81] Gerberich W W, Volinsky A A and Tymiak N I 2000 A brittle to ductile transition in adhered thin films *Mater. Res. Soc. Symp.* **594** 351–63
- [82] Tanaka M, Higashida K, Kishikawa T and Morikawa T 2002 HVEM/AFM observation of hinge-type plastic zones associated with cracks in silicon crystals *Mater. Trans.* **43** 2169–2172
- [83] Zielinski W, Lii M J and Gerberich W W 1992 Crack-tip dislocation arrangements for equilibrium—I. *In situ* TEM observations of Fe-2 wt.% Si *Acta Metall. Mater.* **40** 2861–71
- [84] Marsh P G, Zielinski W, Huang H and Gerberich W W 1992 Crack-tip dislocation emission arrangements for equilibrium. III. Application to large applied stress intensities *Acta Metall. Mater.* **40** 2883–94
- [85] Sun Y, Beltz G F and Rice J R 1993 Estimates from atomic models of tension-shear coupling in dislocation nucleation from a crack-tip *Mater. Sci. Eng. A* **170** 67–85
- [86] Gumbsch P and Beltz G E 1995 On the continuum versus atomistic descriptions of dislocation nucleation and cleavage in nickel *Modelling Simul. Mater. Sci. Eng.* **3** 597–613
- [87] Elsaesser C and Gumbsch P 2005 Crack and interfaces in computers. Ab initio simulations of properties of crystalline materials *Phys. J.* **4** 23–8
- [88] Griffith A A 1920 The phenomena of rupture and flow in solids *Phil. Trans. R. Soc. Lond. A* **221** 163–98
- [89] Kriese M D, Moody N R and Gerberich W W 1998 Effects of annealing and interlayers on the adhesion energy of copper thin films to SiO₂/Si substrates *Acta Mater.* **46** 6623–30
- [90] Peden C H F, Kidd K B and Shinn N P 1991 Metal/metal-oxide interfaces: A surface science approach to the study of adhesion *J. Vac. Sci. Technol. A* **9** 1518–24
- [91] Dauskardt R H, Lane M, Ma Q and Krishna N 1998 Adhesion and debonding of multi-layer thin film structures *Eng. Fract. Mech.* **61** 141–62
- [92] Lane M, Dauskardt R H, Vainchtein A and Gao H 2000 Plasticity contributions to interface adhesion in thin-film interconnect structures *J. Mater. Res.* **15** 2758–69
- [93] Cui Z, Ngo S and Dixit G 2004 A sample preparation method for four point bend adhesion studies *J. Mater. Res.* **19** 1324–7
- [94] Lin Y, Vlassak J J, Tsui T Y and McKerrow A J 2004 Subcritical delamination of dielectric and metal films from low-k organosilicate glass (OSG) thin films in buffered pH solutions *Mater. Res. Soc. Symp. Proc.* **795** 93–8
- [95] Charalambides P G, Lund J, Evans A G and McMeeking R M 1989 A test specimen for determining the fracture resistance of bimaterial interfaces *J. Appl. Mech.* **111** 77–82
- [96] Ma Q, Bumgarner J, Fujimoto H, Lane M and Dauskardt R H 1997 Adhesion measurement of interfaces in multi-layer interconnect structures *Mater. Res. Soc. Symp. Proc.* **473** 3–14
- [97] Suo Z and Hutchinson J W 1989 On sandwiched test specimens for measuring interface crack toughness *Mater. Sci. Eng. A* **107** 135–43
- [98] Lane M and Dauskardt R H 2000 Plasticity contributions to interface adhesion in thin film interconnect structures *J. Mater. Res.* **15** 2758–69
- [99] Lane M W, Snodgrass J M and Dauskardt R H 2001 Environmental effects on interfacial adhesion *Microelectron. Reliab.* **41** 1615–24
- [100] Hughey M P, Morris D J, Cook R F, Bozeman S P, Kelly B L, Chakravarty S L N, Harkens D P and Stearns L C 2004 Four-point bend adhesion measurements of copper and permalloy systems *Eng. Fract. Mech.* **71** 245–61
- [101] Marshall D B and Evans A G 1984 Measurement of adherence of residually stressed thin films by indentation: I. Mechanics of interface delamination *J. Appl. Phys.* **10** 2632
- [102] Rossington C, Evans A G, Marshall D B and Khuri-Yakub B T 1984 Measurements of adherence of residually stressed thin films by indentation: II. Experiments with ZnO/Si *J. Appl. Phys.* **56** 2639–44
- [103] Kriese M D, Moody N R and Gerberich W W 1999 Quantitative adhesion measures of multilayer films: I. Indentation mechanics *J. Mater. Res.* **14** 3007–18
- [104] Kriese M D, Moody N R and Gerberich W W 1999 Quantitative adhesion measures of multilayer films: II. Indentation of W/Cu, W/W, Cr/W *J. Mater. Res.* **14** 3019–26
- [105] DeBoer M P and Gerberich W W 1996 Microwedge indentation of the thin film fine line: I. Mechanics *Acta Mater.* **44** 3169–75
- [106] DeBoer M P and Gerberich W W 1996 Microwedge indentation of the thin film fine line: II. Experimental *Acta Mater.* **44** 3177–87

- [107] Bahr D F and Gerberich W W 1998 Relationships between acoustic emission and energy released during failure events *J. Mater. Res.* **13** 1065–74
- [108] Thouless M D, Hutchinson J W and Linger E G 1992 Plane-strain, buckling-driven delamination of thin films: model experiments and mode-II fracture *Acta Metall. Mater.* **40** 2639–49
- [109] Bagchi A, Lucas G E, Suo Z and Evans A G 1994 A new procedure for measuring the decohesion energy for thin ductile films on substrates *J. Mater. Res.* **9** 1734–41
- [110] Bagchi A and Evans A G 1996 Measurements of the debond energy for thin metallization lines on dielectrics *Thin Solid Films* **286** 203–12
- [111] Moody N R, Adams D P, Cordill M J, Yang N and Bahr D F 2002 The effects of copper on the interfacial failure of gold films *Mater. Res. Soc. Symp. Proc.* **695** 323–8
- [112] Kriese M D, Boismier D A, Moody N R and Gerberich W W 1998 Nanomechanical fracture-testing of thin films *Eng. Fract. Mech.* **61** 1–20
- [113] Kriese M D, Moody N R and Gerberich W W 1998 Quantitative measurement of the effect of annealing on the adhesion of thin copper films using superlayers *Mater. Res. Soc. Symp. Proc.* **505** 363–8
- [114] Volinsky A A, Moody N R and Gerberich W W 2000 Superlayer residual stress effect on the indentation adhesion measurements *Mater. Res. Soc. Symp. Proc.* **594** 383–8
- [115] Kondo I, Takenaka O, Kamiya T, Hayakawa K and Kinbara A 1994 Adhesion measurement of Ti thin films on Si substrate using internal stress in overcoated Ni films *J. Vac. Sci. Technol. A* **12** 169–73
- [116] Moody N R, Medlin D, Boehme D and Norwood D P 1998 Film thickness effects on the fracture of tantalum nitride on aluminium nitride thin film systems *Eng. Fract. Mech.* **61** 107–18
- [117] Moody N R, Hwang R Q, Venkatarman S, Angelo J E, Norwood D P and Gerberich W W 1998 Adhesion and fracture of tantalum nitride films *Acta Mater.* **46** 585–97
- [118] Bahr D F, Hoehn J W, Moody N R and Gerberich W W 1997 Adhesion and acoustic emission analysis of failures in nitride films with a metal interlayer *Acta Mater.* **45** 5163–75
- [119] Cordill M J, Moody N R and Bahr D F 2004 Quantifying improvements in adhesion of platinum films on brittle substrates *J. Mater. Res.* **19** 1818–25
- [120] Hutchinson J W, Thouless M D and Linger E G 1992 Growth and configurational stability of circular, buckling-driven film delaminations *Acta Metall. Mater.* **40** 295–308
- [121] Evans A G and Hutchinson J W 1984 On the mechanics of delamination and spalling in compressed films *Int. J. Solids Struct.* **20** 455–66
- [122] Gioia G and Ortiz M 1998 Determination of thin-film debonding parameters from telephone-cord measurements *Acta Mater.* **46** 169–175
- [123] Cleymand F, Coupeau C and Grille J 2001 Experimental investigation of the instability of buckling patterns: from straight sided to wormlike structures *Scr. Mater.* **44** 2623–27
- [124] Crosby K M and Bradley R M 1999 Pattern formation during delamination and buckling of thin films *Phys. Rev. E* **59** R2542–5
- [125] Jensen H M and Sheinman I 2002 Numerical analysis of buckling-driven delamination *Int. J. Solids Struct.* **39** 3373–86
- [126] Nir D 1984 Stress relief froms of diamond-like carbon thin films under internal compressive stress *Thin Solid Films* **112** 41–9
- [127] Coupeau C 2002 Atomic force microscopy study of the morphological shape of thin film buckling *Thin Solid Films* **406** 190–4
- [128] Audoly B 1999 Stability of Straight delamination blisters *Phys. Rev. Lett.* **83** 4124–427
- [129] Nilsson K F and Giannakopoulos A E 1995 A finite element analysis of configurational stability and finite growth of buckling driven delamination *J. Mech. Phys. Solids* **43** 1983–2021
- [130] Gille G and Rau B 1984 Buckling instability and adhesion of carbon layers *Thin Solid Films* **120** 109–21
- [131] Gioia G and Ortiz M 1997 Delamination of compressed thin films *Adv. Appl. Mech.* **33** 119–92
- [132] Lee A, Clemens B N and Nix W D 2004 Stress induced delamination methods for the study of adhesion of Pt thin films on Si *Acta Mater.* **52** 2081–93
- [133] Cordill M J, Moody N R and Bahr D F 2003 Adhesion of thin ductile films using the stressed overlayer method *TMS Symp. Proc. Surface Engineering in Materials Science II* (Warrendale, PA: TMS Publishing) pp 41–7
- [134] Wei Y and Hutchinson J W 1999 Models of interface separation accompanied by plastic dissipation at multiple scales *Int. J. Fract.* **95** 1–17
- [135] Finnis M W, Stoneham A M and Tasker P W 1989 Approaches to modelling metal/ceramic interfaces *Metal-Ceramic Interfaces Proceedings of an International Workshop* ed M Rühle *et al* (New York: Pergamon) pp 35–44
- [136] Beltz G E and Rice J R 1992 Dislocation nucleation at metal-ceramic interfaces *Acta Metall. Mater.* **40** S321–31

- [137] Wang J S 1998 A micromechanical model for interface crack extension in metal/ceramic bimaterial systems *Acta Mater.* **46** 4973–84
- [138] Lane M W, Liu X H and Shaw T M 2004 Environmental effects on cracking and delamination of dielectric films *IEEE Device Mater. Reliab.* **4** 142–7
- [139] Wang H F, Gerberich W W and Skowronek C J 1993 Fracture mechanics of Ti/Al₂O₃ interfaces *Acta Metall. Mater.* **41** 2425–32
- [140] Moody N R, Adams D P, Medlin D, Headley T, Yang N and Volinsky A A 2003 Effects of diffusion on interfacial fracture of gold-chromium hybrid microcircuit films *Int. J. Fract.* **119–120** 407–19
- [141] Cordill M J, Muppidi T, Moody N R and Bahr D F 2004 Effects of microstructure on the mechanical properties of copper films for high aspect ratio structures *Microsyst. Technol.* **10** 451–55
- [142] Cordill M J, Moody N R, Adams D P, Yang N, Bahr D F and Gerberich W W 2005 Environmental effects on the adhesion of gold microcircuit films, in preparation
- [143] Gerberich W W, Tymiak N I, Jungk J M and Wyrobek, T 2004 Hydrogen effects on mechanical response of small volumes *Hydrogen Effects on Material Behavior and Corrosion Deformation Interactions* ed N R Moody *et al* (Warrendale, PA: TMS Publishing) pp 153–64
- [144] Moody N R, Causey R A, Wilson K L and Bahr D F 2004 Hydrogen-induced fracture of sputter deposited beryllium films *Hydrogen Effects on Material Behavior and Corrosion Deformation Interactions* ed N R Moody *et al* (Warrendale, PA: TMS Publishing) pp 363–72
- [145] Moody N R, Angelo J E, Foiles S M, Baskes M I and Gerberich W W 1993 Application of atomistic simulations to the hydrogen-induced fracture process of an iron-based superalloy *6th Israel Materials and Engineering Conf.* ed N R Moody *et al* (Warrendale, PA: TMS Publishing) pp 544–8
- [146] Moody N R, Baskes M I, Robinson S L and Perra M W 2001 Temperature effects on hydrogen-induced crack growth susceptibility of iron based superalloys *Eng. Frac. Mech.* **68** 731–50
- [147] Perra M W 1981 Substained-local cracking of austenitic steels in gaseous hydrogen *Proc. 2nd Int. Conf. on Environmental Degradation of Materials* vol 2, ed M R Louthan Jr *et al* (Blacksburg, VA: Virginia Polytechnic Institute) pp 321–33
- [148] Cordill M J, Bahr D F, Moody N R and Gerberich W W 2004 Recent developments in thin film adhesion measurements *IEEE Trans. Device Mater. Reliab.* **4** 163–8
- [149] Mao S X and Evans A G 1997 The influence of blunting on crack growth at oxide/metal interfaces *Acta Mater.* **45** 4263–70
- [150] Tymiak N I, Volinsky A A, Kriese M D, Downs S A and Gerberich W W 2000 The role of plasticity in bimaterial fracture with ductile interlayers *Metall. Mater. Trans. A* **31** 863–72
- [151] Dehm G, Ruhle M, Conway H D and Raj R 1997 A microindentation method for estimating shear strength and its use in studying the influence of titanium transition layers on the interface strength of epitaxial copper films on sapphire *Acta Metall.* **45** 489–99
- [152] Bahr D F, Woodcock C L, Pang M, Weaver K D and Moody N R 2003 Indentation induced film fracture in hard film-soft substrate systems *Int. J. Frac.* **119–120** 339–49
- [153] Manson S S 1954 *NACA Report 1170* Lewis Flight Propulsion Laboratory Cleveland, OH
- [154] Coffin L F Jr 1954 A study of the effects of cyclic thermal stresses on a ductile metal *Trans. ASME* **76** 931–50
- [155] Kohlhoff S, Gumbsch P and Fischmeiser H F 1991 Crack Propagation in bcc crystals studied with a combined finite-element and atomistic model *Phil. Mag. A* **64** 851–78
- [156] Gumbsch P J 1995 An atomistic study of brittle fracture: toward explicit failure criteria from atomistic modelling *J. Mater. Res.* **10** 2897–907
- [157] Shastry V, Anderson P M and Thomson R 1994 Nonlocal effects of existing dislocations on crack-tip emission and cleavage *J. Mater. Res.* **9** 812–27
- [158] Rose J H, Smith J R and Ferrante J 1983 Universal features of bonding in metals *Phys. Rev. B* **28** 1838–45
- [159] Smith J R, Schlosser H and Ferrante J 1989 Universal energy relations and metal/ceramic interfaces *Metal–Ceramic Interfaces Proc. Int. Workshop, Santa Barbara, CA, 16–18 January 1989* ed M Ruhle *et al* (New York: Pergamon) pp 15–24
- [160] Smith J R, Reynolds J E, Roddick E R and Srolovitz D J 1996 An atomistic view of adhesion *J. Comput. Aided Mater. Des.* **3** 169–72
- [161] Tadmor E B, Ortiz M and Phillips R 1996 Quasicontinuum analysis of defects in solids *Phil. Mag. A* **73** 1529–63
- [162] Miller R, Tadmor E B, Phillips R and Ortiz M 1998 Quasicontinuum simulation of fracture at the atomic scale *Modelling Simul. Mater. Sci. Eng.* **6** 607–38
- [163] Ortiz M and Phillips R 1999 Nanomechanics of defects in solids *Adv. Appl. Mech.* **36** 1–79
- [164] Broughton J Q, Abraham F F, Bernstein N and Kaxiras E 1999 Concurrent coupling of length scales: methodology and application *Phys. Rev. B* **60** 2391–403

- [164] Bulatov V V and Kaxiras E 1997 Semidiscrete variational Peierls framework for dislocation core properties *Phys. Rev. B* **78** 4221–4
- [165] Zbib H M, de la Rubia T D, Rhee M and Hirth J P 2000 3D dislocation dynamics: stress-strain behaviour and hardening mechanisms in FCC and BCC metals *J. Nucl. Mater.* **276** 154–65
- [166] Ramasubramanian A, Curtin W A and Farkas D 2002 Fracture in nanolamellar materials: continuum and atomistic models with application to titanium aluminides *Phil. Mag. A* **82** 2397–417
- [167] Farkas D, Nogueira R, Ruda M and Hyde B 2005 Atomistic simulations of the effects of segregated elements on grain-boundary fracture in body-centered-cubic Fe *Metall. Mater. Trans. A* **36** 2067–72
- [168] Miller R, Ortiz M, Phillips R, Shenoy V and Tadmor E B 1998 Quasicontinuum models of fracture and plasticity *Eng. Fract. Mech.* **61** 427–44
- [169] Stillinger F H and Weber T A 1983 Computer simulations of local order in condensed phases of silicon *Phys. Rev. B* **31** 5262–71
- [170] Tersoff J 1988 Empirical interatomic potential for silicon with improved elastic properties *Phys. Rev. B* **38** 9902–5
- [171] Hugo R C, Kung H, Weertman J R, Mitra R, Knapp J A and Follstaedt D M 2003 In-situ TEM tensile testing of DC magnetron sputtered and pulsed laser deposited Ni thin films *Acta Mater.* **51** 1937–43
- [172] Kumar K S, Van Swygenhöven H and Suresh S 2003 Mechanical behaviour of nanocrystalline metals and alloys *Acta Mater.* **51** 5743–74
- [173] Pettifor D G 2003 Electron theory in materials modelling *Acta Mater.* **51** 5643–73
- [174] Li J, Ngan A H W and Gumbsch P 2003 Atomistic modelling of mechanical behaviour *Acta Mater.* **51** 5711–42
- [175] Rice J R and Thomson R 1974 Ductile versus brittle behaviour of crystals *Phil. Mag.* **29** 73–97
- [176] Masuda-Jindo K, Zhou S J, Thomson R and Carlsson A E 1994 Atomic theory of fracture of crystalline materials: cleavage and dislocation emission criteria *Mater. Sci. Eng. A* **176** 255–61